INTERNATIONAL JOURNAL FOR NUMERICAL METHODS IN ENGINEERING
Int. J. Numer. Meth. Engng 2004; **60**:2467–2499 (DOI: 10.1002/nme.1054)

A spectral-element method for modelling cavitation in transient fluid–structure interaction

M. A. Sprague*, † and T. L. Geers

Mechanical Engineering, University of Colorado, Boulder, CO 80309-0427, U.S.A.

SUMMARY

In an underwater-shock environment, cavitation (boiling) occurs as a result of reflection of the shock wave from the free surface and/or wetted structure causing the pressure in the water to fall below its vapour pressure. If the explosion is sufficiently distant from the structure, the motion of the fluid surrounding the structure may be assumed small, which allows linearization of the governing fluid equations. In 1984, Felippa and DeRuntz developed the cavitating acoustic finite-element (CAFE) method for modelling this phenomenon. While their approach is robust, it is too expensive for realistic 3D simulations. In the work reported here, the efficiency and flexibility of the CAFE approach has been substantially improved by: (i) separating the total field into equilibrium, incident, and scattered components, (ii) replacing the bilinear CAFE basis functions with high-order Legendre-polynomial basis functions, which produces a cavitating acoustic spectral element (CASE) formulation, (iii) employing a simple, non-conformal coupling method for the structure and fluid finite-element models, and (iv) introducing structure–fluid time-step subcycling. Field separation provides flexibility, as it admits non-acoustic incident fields that propagate without numerical dispersion. The use of CASE affords a significant reduction in the number of fluid degrees of freedom required to reach a given level of accuracy. The combined use of subcycling and non-conformal coupling affords order-of-magnitude savings in computational effort. These benefits are illustrated with 1D and 3D canonical underwatershock problems. Copyright © 2004 John Wiley & Sons, Ltd.

KEY WORDS: underwater shock; field separation; non-conformal coupling; time-step subcycling

1. BACKGROUND AND MOTIVATION

In the context of fluid–structure interaction (FSI) pertaining to underwater shock, cavitation occurs as a result of the reflection of the shock wave from the free surface and/or wetted structure, which causes the pressure in the water to fall below its vapour pressure [1]. The instantaneous bulk modulus of cavitated water is orders of magnitude smaller than that of

*Correspondence to: M. A. Sprague, Applied Mathematics, University of Colorado at Boulder, Boulder, CO 80309-0526, U.S.A.
†E-mail: michael.sprague@colorado.edu

Contract/grant sponsor: Office of Naval Research and the Naval Surface Warfare Center, Carderock; contract/grant number: N00014-01-1-0154

Received 18 July 2003
Revised 29 August 2003
Accepted 2 January 2004

Published online 2 July 2004

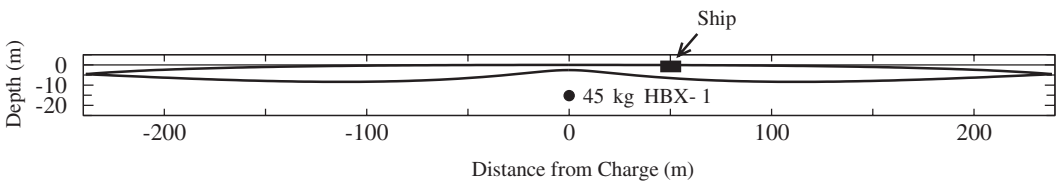

Figure 1. Cavitation-region envelope for a 45 kg charge of HBX-1 detonated at a 15 m depth. Also, shown is the aft view of a box-like ship with 9.1 m beam, 4.6 m height and 3.1 m draft.

uncavitated water, which produces non-linear material behaviour. A simple but satisfactory constitutive model is a bilinear one, in which the bulk modulus is that of water as an acoustic medium when the condensation (roughly, negative volume strain) is positive, and zero when the condensation is negative [2]. Although pure water has been found to sustain substantial negative pressures, even small amounts of dissolved gases nullify the effect [3].

Near-free-surface underwater-shock problems are further complicated by the existence of three greatly different spatial scales: the size of the ship, the decay length of the incident wave, and the spatial extent of the cavitation. This is best illustrated by an example: a 45 kg charge of HBX-1 detonated at a depth of 15 m yields a cavitation region with maximum diameter 489 m and maximum depth 9 m [4]. This region is shown with a representative ship in Figure 1. The associated $1/e$ decay length of the shock wave when it reaches the ship is 0.9 m [5, 6].

1.1. Cavitating acoustic finite-elements (CAFE)

1.1.1. CAFE approach. When the underwater explosion is sufficiently removed from the structure, the motion of the fluid surrounding the structure is small, which allows the fluid to be treated as acoustic but subject to cavitation. In 1984, Felippa and DeRuntz [7] developed a cavitating acoustic finite-element (CAFE) for FSI calculations based on the work of Newton [8–11], in which the wave field in the fluid is represented by a scalar displacement potential. Trilinear, isoparametric, eight-node brick elements were formulated; a six-node wedge element was added later [12]. The CAFE semi-discrete equations were integrated in time with a central-difference algorithm. Cavitation was treated node-by-node in an on/off fashion in the time-update equations. Numerical damping was employed to suppress the occurrence of spurious cavitation, which they called *frothing*; the damping also had a beneficial effect on structure responses in an acoustic fluid, as oscillatory numerical artifacts were smoothed. Their choice of explicit time integration over unconditionally stable implicit integration seems appropriate because the time scales associated with the incident wave and cavitation are typically very small [13].

The CAFE solution strategy for a ship-shock simulation consists of four steps (Figure 2): (i) construct a finite-element (FE) model of the structure, (ii) interface it with a CAFE model of the fluid region in which cavitation is expected to occur, (iii) enclose the CAFE mesh with a non-reflecting boundary and (iv) start integrating the CAFE equations just before the incident wavefront reaches either the free surface of the fluid or the wet surface of the structure [7, 14].

CAFEs were first implemented in the cavitating fluid analysis (CFA) code [7], with the structure equations being handled by the structural analysis of general shells (STAGS) [15]

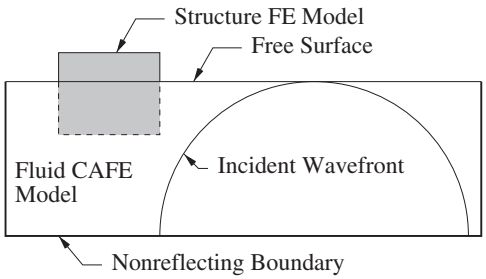

Figure 2. FE/CAFE/non-reflecting-boundary approach for ship-shock simulations; incident wavefront shown just before the onset of cavitation.

finite-element program. The fluid mesh was bounded by a first-order doubly asymptotic approximation (DAA) [16, 17], as implemented in the underwater shock analysis (USA) code [18]. A staggered-time-integration procedure [19] was used, in which the structure equations were integrated with an implicit trapezoidal-rule scheme. A similar approach is used in the NASTRAN-CFA-DAA code [14, 20]. The CAFE approach has been implemented in LS-DYNA/USA [18, 21] (the MAT90 element formulation), where the fluid and structure semi-discrete equations are integrated explicitly, and the fluid mesh is bounded by a DAA or plane-wave-approximation boundary. A similar CAFE formulation is currently being incorporated into ABAQUS [22, 23], where the fluid domain is truncated by a curved-wave-approximation (CWA) boundary.

For problems in which the underwater explosion is near or in contact with the structure, the fluid motion can no longer be considered small. In this case, a hydrocode [24] must be used, which is much more expensive per unit volume of fluid, but is required only for localized analysis.

1.1.2. Deficiencies of the CAFE approach. Although the approach of Felippa and DeRuntz [7] is well developed, it has deficiencies that make it too expensive for accurate 3D simulations. First, CAFEs exhibit high numerical dispersion due to their use of low-order basis functions [25]; high mesh refinement is typically required. With the occurrence of cavitation, a phenomenon that is highly local in space and time, the refinement requirement is extreme. The need for a 'super-refined' mesh is demonstrated in 1D and 2D problems by Sprague and Geers [13] and by Sprague [26].

Also demonstrated in Sprague and Geers [13] is that the integration of CAFE equations with a time increment substantially smaller than the critical time increment for stable integration produces spurious regions of cavitation. In an explicit-fluid/explicit-structure implementation with one-to-one fluid–structure nodal coupling, the critical time increment for the structure equations is typically much smaller than that required for the fluid equations because the sound speed in steel is more than three times that in water. In a CAFE/FE implementation where the structure and fluid equations are integrated with the same time increment [7, 21], integration of the fluid equations with a too-small time increment is often unavoidable.

The CFA [7] and LS-DYNA [21] implementations feature one-to-one coupling between the fluid and structural nodes at their interface. Thus, fluid-mesh refinement requires structure-mesh refinement; if the structure mesh is already adequately refined, this constitutes a waste of

computer resources. Furthermore, if the CAFE implementation employs explicit-fluid/explicit-structure time integration, the structure-FE critical time increment is also reduced with mesh refinement. In the ABAQUS implementation [22], the requirement for one-to-one structure–fluid nodal coupling has been removed by a sophisticated membrane-coupling approach that allows an arbitrary CAFE mesh to be coupled to an arbitrary structure mesh.

For accurate simulation, Felippa and DeRuntz [7] recommend that the CAFE mesh encompass all regions of fluid that experience cavitation. However, this is an impractical recommendation for most near-free-surface shock problems because the size of the cavitation region is extremely large relative to the decay length of the incident wave. A CAFE mesh that is sufficiently refined to model accurately the incident wave and that also encompasses the entire cavitation region is untenable.

Finally, Felippa and DeRuntz [7] recommend that time integration begin before the incident wavefront contacts the structure or causes regions of cavitation, which can produce the situation illustrated in Figure 2. There, the incident wavefront (which is usually discontinuous) must be propagated an appreciable distance through the dispersive mesh before reaching the structure, thereby distorting the incident wave as it travels.

1.2. Improvements to the CAFE approach

Here, we describe four improvements that combine to make the CAFE approach a viable treatment for 3D near-free-surface shock analysis. These improvements are:

- introduction of field separation,
- replacement of the trilinear basis functions (finite-element method) with Legendre-polynomial basis functions (spectral-element method),
- incorporation of a novel non-conformal fluid–structure coupling method,
- implementation of fluid–structure subcycling.

1.2.1. Field separation. The far field produced by an acoustic shock wave in an unbounded fluid (the incident field) is relatively easy to define [27] and is typically known in closed form. This presents two opportunities:

- the discontinuous wave may be propagated without numerical dispersion,
- the incident wave may be propagated ‘quasi-acoustically’, in conformance with experimental data [27, 28].

In order to exploit these opportunities, we employ a technique used frequently in linear scattering problems: separating the total field into a known incident field and an unknown scattered field, and employing the fluid mesh to calculate the scattered field only. The technique has been applied to transient FE FSI calculations by Chan [29, 30] and is also implemented in ABAQUS [22]. It has also been applied to transient finite-difference electrodynamics calculations [31].

Recently, a 1D implementation of field-separation was used to demonstrate that, when the simulation is started with the incident wavefront very close to the structure, field separation neither improves nor degrades the structure response [32]. Here, we investigate the efficacy of field separation when applied to 3D FSI calculations in an acoustic fluid with and without the occurrence of cavitation.

1.2.2. Cavitating acoustic spectral elements. As discussed above, a fundamental limitation of low-order elements is the high numerical dispersion produced in wave-propagation problems; this is exacerbated when the field contains discontinuities, as in underwater-shock problems. Convergence is attained by refinement of the mesh (h-refinement). With high-order schemes, convergence may be attained with a combination of h-refinement and an increase of element order (p-refinement). High-order elements generate less dispersion, but have traditionally been avoided for two reasons [33]: (i) they typically produce higher maximum mesh eigenvalues, thus decreasing the critical time increment for explicit integration, and (ii) they often produce more troublesome spurious oscillations when applied to wave-propagation problems with solution discontinuities. However, the reduced dispersion can more than compensate for the presence of the oscillations and reduced critical time increment [34]. This is clearly shown in [35], where a numerical example is used to illustrate that information is contained in these oscillations and that high-order schemes retain more information than low-order schemes.

The spectral-element method (SEM) combines the accuracy of spectral methods [36–39] with the geometric flexibility of the finite-element method (FEM) [33]. The most effective spectral elements (SEs) appear to be the Legendre-polynomial-based elements [40, 41], which display impressive wave-propagation capabilities [34, 42]. For problems with regular domains and adequately smooth solutions, the SEM enjoys exponential convergence; this is lost when the solution contains discontinuities, as examined in several investigations [35, 43–45]. Finally, spectral methods are well suited to parallel-CPU implementation [46].

The SEM was first introduced by Patera [47], who applied the method to the incompressible Navier–Stokes equations in 1D and 2D. While most of the early work with the SEM used SEs with Chebyshev-polynomial basis functions [47–51], Legendre polynomials [40, 41, 46, 52] have emerged as the preferred basis functions. This is because Legendre basis functions with Gauss–Lobatto–Legendre quadrature:

- allow fast matrix–vector-product evaluation with tensor-product factorization [41],
- produce diagonal mass matrices [40],
- yield matrices with better conditioning and sparsity relative to those produced with Chebyshev basis functions [42, 46],
- exhibit convergence rates comparable to those for Chebyshev polynomials [40].

In a recent investigation [32], we demonstrated that a 1D implementation of CASE provided significant savings in terms of required fluid degrees of freedom and memory storage for a given level of accuracy. In terms of computational operations, the requirements of CASE and CAFE were comparable. Here, we use a 3D implementation to compare CASE and CAFE in terms of computational resources required to achieve a fixed level of accuracy. These resources pertain to (i) fluid-model degrees-of-freedom, (ii) memory storage and (iii) CPU effort.

1.2.3. Fluid–structure coupling. The CAFE approach is best utilized if the fluid and structure meshes can be refined separately. To this end, we propose a novel coupling method that is considerably simpler than that used in the ABAQUS implementation [22]. With this method, the fluid may be refined to an arbitrary level without requiring a change in the structure mesh.

While there are several methods for coupling two geometrically different meshes [53, 54], the method used here, which may be classified as consistent-interpolation coupling [53], is simple in terms of implementation. The gains associated with more complex coupling, which

may be 'mathematically optimal', are small and not worth the associated computational cost for the class of problems studied here [53].

1.2.4. Fluid–structure subcycling. Time-step subcycling [55–57] is a simple technique that is suitable for CAFE/FE staggered time integration. It allows both the structure and fluid equations to be integrated with near-optimal time increments. In the approach used here, the fluid equations are updated at an integer multiple or division of the time increment for the structure equations. This is a valuable improvement, as it allows gains in accuracy with considerable reduction of computational cost.

2. FORMULATION AND IMPLEMENTATION

2.1. Continuum fluid models

We address the underwater shock problem illustrated in Figure 2. We assume that fluid motion is inviscid and irrotational, thus allowing a potential representation of the field. As discussed in Section 1, the fluid model uses a bilinear constitutive relation [2] to account for cavitation, which is such that the fluid cannot transmit negative pressures and cavitation is treated as a macroscopically homogeneous phenomenon.

In an underwater shock problem, the total field may be represented as the sum of three fields: equilibrium, incident and scattered. The equilibrium field is easily determined as that due to atmospheric plus hydrostatic pressure, the incident field is less easily determined as that due to a quasi-acoustic shock wave propagating in a homogeneous, unbounded fluid and the complicated scattered field is caused by the presence of both the structure and the free surface. We consider two models for the field. The first is called the total-field model (TFM) because its dependent variables are composed of incident and scattered quantities. The second model is called the scattered-field model (SFM), as it treats only the scattered field on the assumption that the incident field is known for all time throughout the domain.

2.1.1. Total-field model. In deriving the governing equations for the acoustic fluid subject to cavitation, we begin with the bilinear equation of state [2],

$$p = p_v + \begin{cases} B_a(\rho/\rho_a - 1), & \rho \geqslant \rho_a \\ 0, & \rho < \rho_a \end{cases} \tag{1}$$

which is illustrated in Figure 3. Here, B_a is the bulk modulus of the acoustic fluid in the absence of cavitation, $p(\boldsymbol{X}, t)$ is the total pressure in the fluid, p_v is the vapour pressure of water at temperature T_0, ρ_a is the corresponding density of the saturated liquid, and $\rho(\boldsymbol{X}, t)$ is the instantaneous density; $\boldsymbol{X}$ is the global-position vector and t denotes time. We assume that T_0, ρ_a and p_v are constant throughout the domain of interest. By definition, $B_a = \rho_a c^2$, where c is the sound speed in the uncavitated acoustic fluid, and $S = (\rho/\rho_a - 1)$ is the total condensation. These definitions allow us to rewrite the equation of state as

$$p = p_v + \begin{cases} \rho_a c^2 S, & S \geqslant 0 \\ 0, & S < 0 \end{cases} \tag{2}$$

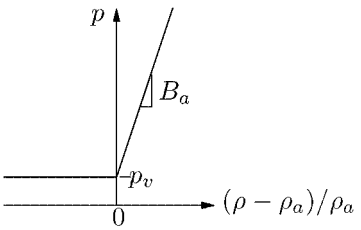

Figure 3. Bilinear equation of state for an acoustic fluid subject to cavitation.

The continuity equation may be written [58]

$$\frac{\partial \rho}{\partial t} + \boldsymbol{\nabla} \cdot \left(\rho \frac{\partial \boldsymbol{u}}{\partial t} \right) = 0 \tag{3}$$

where $\boldsymbol{u}(\boldsymbol{X}, t)$ is the total fluid displacement. If $|S| \ll 1$, (3) becomes

$$\frac{\partial S}{\partial t} + \boldsymbol{\nabla} \cdot \frac{\partial \boldsymbol{u}}{\partial t} = 0 \tag{4}$$

The Euler momentum equation [58], which pertains to inviscid flow, may be written

$$\frac{\partial^2 \boldsymbol{u}}{\partial t^2} + \left(\frac{\partial \boldsymbol{u}}{\partial t} \cdot \boldsymbol{\nabla} \right) \frac{\partial \boldsymbol{u}}{\partial t} = \frac{1}{\rho} \boldsymbol{\nabla} p - \boldsymbol{\nabla} V_g \tag{5}$$

where $V_g(\boldsymbol{X})$ is the gravity-potential field. If $|S| \ll 1$ and the convective term is much smaller than the inertial term, (5) becomes

$$\rho_a \frac{\partial^2 \boldsymbol{u}}{\partial t^2} = -\boldsymbol{\nabla} p - \rho_a \boldsymbol{\nabla} V_g \tag{6}$$

Since fluid motion is assumed irrotational, we may write the total displacement field as

$$\boldsymbol{u} = -\boldsymbol{\nabla} \Psi + \boldsymbol{u}_{\text{eq}} \tag{7}$$

where $\Psi(\boldsymbol{X}, t)$ is the dynamic *displacement potential* and $\boldsymbol{u}_{\text{eq}}(\boldsymbol{X})$ is the equilibrium displacement field. We utilize (7) to write the continuity equation (4) as

$$\frac{\partial S}{\partial t} - \nabla^2 \frac{\partial \Psi}{\partial t} = 0 \tag{8}$$

which may be integrated in time to yield

$$S = \nabla^2 \Psi + S_{\text{eq}} \tag{9}$$

where $S_{\text{eq}}(\boldsymbol{X})$ is the equilibrium condensation field. Similarly, the momentum equation (6) may be written

$$\boldsymbol{\nabla} \frac{\partial^2 \Psi}{\partial t^2} = \frac{1}{\rho_a} \boldsymbol{\nabla} p + \boldsymbol{\nabla} V_g \tag{10}$$

which may be integrated in space to yield

$$\frac{\partial^2 \Psi}{\partial t^2} = \frac{1}{\rho_a} p + V_g + h \tag{11}$$

where $h(t)$ is a 'constant' of integration. If we consider the equilibrium problem, (11) becomes

$$\frac{\partial^2 \Psi}{\partial t^2} = \frac{1}{\rho_a} (p - p_{\text{eq}}) \tag{12}$$

where $p_{\text{eq}} = -\rho_a (V_g + h)$ is the equilibrium pressure, i.e. the sum of atmospheric pressure and hydrostatic pressure. The introduction of (2) into (12) then yields

$$\rho_a \frac{\partial^2 \Psi}{\partial t^2} = -p_{\text{eq}} + p_v + \begin{cases} \rho_a c^2 S, & S \geqslant 0 \\ 0, & S < 0 \end{cases} \tag{13}$$

Now, if we utilize $p_{\text{eq}} = p_v + \rho_a c^2 S_{\text{eq}}$, define the dynamic *densified condensation* $s = \rho_a (S - S_{\text{eq}})$, and the *densified displacement potential* $\psi = \rho_a \Psi$, we may write from (9) and (13) the system of governing equations

$$s = \nabla^2 \psi, \quad \ddot{\psi} = \begin{cases} c^2 s, & c^2 s \geqslant p_v - p_{\text{eq}} \\ p_v - p_{\text{eq}}, & c^2 s < p_v - p_{\text{eq}} \end{cases} \tag{14}$$

where an overdot denotes a temporal partial derivative. The use of these scalar field quantities, as opposed to vector quantities, minimizes the number of unknowns at each point in the fluid domain and enforces irrotationality of the flow. The fluid domain governed by (14) has essential boundary conditions at the free surface and natural boundary conditions along the interface with the structure and the non-reflecting boundary.

The vapour pressure of the water is so much smaller than the equilibrium pressure that it may be neglected. For example, at 10°C the vapour pressure of water is approximately 10^3 Pa, whereas the minimum equilibrium pressure, i.e., atmospheric pressure, is 10^5 Pa.

2.1.2. Scattered-field model. Here, we separate the total field into three component fields: equilibrium, incident and scattered. Hence, we write $s = s_{\text{inc}} + s_{\text{sc}}$ and $\psi = \psi_{\text{inc}} + \psi_{\text{sc}}$, where all of these variables constitute deviations from equilibrium.

Introducing $s = s_{\text{inc}} + s_{\text{sc}}$ and $\psi = \psi_{\text{inc}} + \psi_{\text{sc}}$ into (14), we obtain the scattered-field model

$$s_{\text{sc}} = \nabla^2 \psi_{\text{sc}} + \varepsilon_1, \quad \ddot{\psi}_{\text{sc}} = \begin{cases} c^2 s_{\text{sc}} + \varepsilon_2, & c^2 s_{\text{sc}} > -(p_{\text{eq}} + p_{\text{inc}}) \\ -(p_{\text{eq}} + p_{\text{inc}}), & c^2 s_{\text{sc}} \leqslant -(p_{\text{eq}} + p_{\text{inc}}) \end{cases} \tag{15}$$

where $p_{\text{inc}} = \ddot{\psi}_{\text{inc}}$ is the incident pressure and

$$\varepsilon_1 = \nabla^2 \psi_{\text{inc}} - s_{\text{inc}}, \quad \varepsilon_2 = c^2 s_{\text{inc}} - \ddot{\psi}_{\text{inc}} \tag{16}$$

Because $|s_{\text{inc}}| \ll 1$, and because the fluid motion is irrotational and inviscid, $s_{\text{inc}} = \nabla^2 \psi_{\text{inc}}$, which produces $\varepsilon_1 = 0$. If the incident field propagates acoustically, we may write from (14)

$$\ddot{\psi}_{\text{inc}} = c^2 s_{\text{inc}} \tag{17}$$

which produces $\varepsilon_2 = 0$. Note that the second of (15) involves a dynamic quantity on the right sides of the inequalities, in contrast to the second of (14). In addition, the free-surface (FS) essential boundary condition for the scattered-field equations is time dependent, i.e.

$$p_{\mathrm{sc}}|_{\mathrm{FS}} + p_{\mathrm{inc}}|_{\mathrm{FS}} = 0 \tag{18}$$

An important advantage of the scattered-field model over the total-field model is the opportunity to propagate *any* incident field through the fluid domain with total fidelity. For example, Hunter and Geers [27] recently developed a realistic field model in which the shock wave propagates quasi-acoustically, i.e. the wavefront propagates with the fluid sound speed, but the waveform slowly distorts as it travels. Although incorporation of such a model violates the acoustic-field assumption in (17), ε_2 is negligible locally, and may be ignored.

2.2. Spatial discretization

2.2.1. CASE: total-field model. We seek to construct cavitating acoustic spectral elements (CASE) based on the irrotational-flow formulation of Newton [8–11]. A subparametric discretization is used: first-order (trilinear) basis functions are used for geometry representation and higher-order basis functions are used for field-variable representation. The finite fluid volume Ω_{fl} is separated into n_e hexagonal elements defined by eight corner points. The geometry within each element is expressed as

$$X = \boldsymbol{\varphi}^{\mathrm{T}}(\xi, \eta, \zeta)\mathbf{X}, \quad Y = \boldsymbol{\varphi}^{\mathrm{T}}(\xi, \eta, \zeta)\mathbf{Y}, \quad Z = \boldsymbol{\varphi}^{\mathrm{T}}(\xi, \eta, \zeta)\mathbf{Z} \tag{19}$$

where $\mathbf{X}, \mathbf{Y}, \mathbf{Z}$ are column vectors of element-corner-point locations in global co-ordinates, $\boldsymbol{\varphi}$ is a column vector of standard trilinear shape functions (see, e.g. Reference [33]), a T superscript denotes vector transposition, and (ξ, η, ζ) are the element natural co-ordinates $(-1 \leqslant \xi, \eta, \zeta \leqslant 1)$.

The dependent field variables are represented within each element as

$$\begin{aligned} s(\xi, \eta, \zeta, t) &= \boldsymbol{\phi}^{\mathrm{T}}(\xi, \eta, \zeta)\mathbf{s}^e(t) = \sum_{i,j,k=0}^{N} \phi_i(\xi)\phi_j(\eta)\phi_k(\zeta)s^e_{ijk}(t) \\ \psi(\xi, \eta, \zeta, t) &= \boldsymbol{\phi}^{\mathrm{T}}(\xi, \eta, \zeta)\boldsymbol{\psi}^e(t) = \sum_{i,j,k=0}^{N} \phi_i(\xi)\phi_j(\eta)\phi_k(\zeta)\psi^e_{ijk}(t) \end{aligned} \tag{20}$$

where $\mathbf{s}^e$ and $\boldsymbol{\psi}^e$ are column vectors of $(N+1)^3$ time-dependent nodal values (s^e_{ijk} and ψ^e_{ijk}), and $\boldsymbol{\phi}$ is a column vector composed of 1D, Nth-order-polynomial basis functions $\phi_i(\xi)\phi_j(\eta)\phi_k(\zeta)$. The essence of the spectral-element method lies in the choice of ϕ_i and the associated quadrature rule; here, we use Lagrangian interpolants given by [40]

$$\phi_i(\xi) = -\frac{(1-\xi^2)P'_N(\xi)}{N(N+1)P_N(\xi_i)(\xi - \xi_i)} \tag{21}$$

where P_N is the Legendre polynomial of degree N, the prime denotes differentiation with respect to argument, and ξ_i is the ith Gauss–Lobatto–Legendre (GLL) quadrature point defined by the corresponding root of

$$(1-\xi^2)P'_N(\xi) = 0 \tag{22}$$

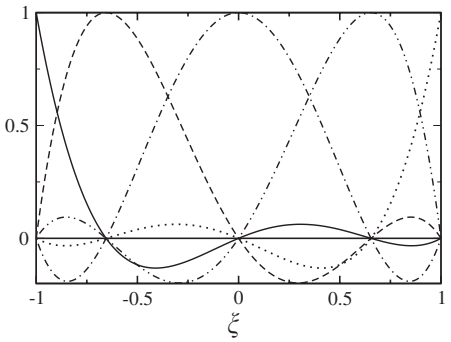

Figure 4. 1D Lagrangian interpolants based on Legendre polynomials for $N = 4$ refinement.

Expression (21) satisfies the relation [40]

$$\phi_i(\xi_j) = \delta_{ij} \tag{23}$$

where δ_{ij} is the Kronecker delta. The 1D Lagrangian interpolants (21) are shown in Figure 4 for $N = 4$. Element-node locations are coincident with the quadrature points, which are located at the $(N+1)$ zeroes of (22). Finally, the expressions for the derivative of (21) when evaluated at GLL quadrature points may be written as [39]

$$\left.\frac{\partial \phi_i}{\partial \xi}\right|_{\xi=\xi_j} = \begin{cases} \dfrac{P_N(\xi_j)}{P_N(\xi_i)} \dfrac{1}{\xi_j - \xi_i}, & i \neq j \\ -\dfrac{(N+1)N}{4}, & i = j = 0 \\ \dfrac{(N+1)N}{4}, & i = j = N \\ 0, & \text{otherwise} \end{cases} \tag{24}$$

The governing equations for the TFM (14a) are discretized with a standard Galerkin approach [33]: premultiplication of (14a) by $\boldsymbol{\phi}$, integration over the element fluid volume, and application of Green's first identity. This yields

$$\int_{\Omega^e} \boldsymbol{\phi} s \, \mathrm{d}\Omega + \int_{\Omega^e} \boldsymbol{\nabla}\boldsymbol{\phi} \cdot \boldsymbol{\nabla}\psi \, \mathrm{d}\Omega = \int_{\Gamma^e} \boldsymbol{\phi} \boldsymbol{\nabla}\psi \cdot \boldsymbol{n} \, \mathrm{d}\Gamma \tag{25}$$

where Ω^e is the element domain, Γ^e is its surface and $\boldsymbol{n}(\boldsymbol{X})$ is the outward unit vector normal to Γ^e. Substitution of (20) into the dependent variables on the left-hand side of (25) yields the element-level algebraic equations

$$\mathbf{Q}^e \mathbf{s}^e + \mathbf{H}^e \boldsymbol{\psi}^e = \mathbf{b}^e \tag{26}$$

where the capacitance matrix, reactance matrix and boundary-interaction vector are given by

$$\mathbf{Q}^e = \int_{\Omega^e} \boldsymbol{\phi}\boldsymbol{\phi}^{\mathrm{T}} \, \mathrm{d}\Omega, \quad \mathbf{H}^e = \int_{\Omega^e} \boldsymbol{\nabla}\boldsymbol{\phi} \cdot \boldsymbol{\nabla}\boldsymbol{\phi}^{\mathrm{T}} \, \mathrm{d}\Omega, \quad \mathbf{b}^e = \int_{\Gamma^e} \boldsymbol{\phi} \boldsymbol{\nabla}\psi \cdot \boldsymbol{n} \, \mathrm{d}\Gamma \tag{27}$$

respectively. Both $\mathbf{Q}^e$ and $\mathbf{H}^e$ are symmetric. Note that $\nabla\psi$ is maintained in its continuum form for $\mathbf{b}^e$ because it is provided by the displacements at the structure and non-reflecting boundaries.

The element-level equations may be assembled into a global system; the resulting semi-discrete equations are

$$\mathbf{Q}\mathbf{s} + \mathbf{H}\boldsymbol{\psi} = \mathbf{b} \tag{28}$$

where $\mathbf{Q}$ and $\mathbf{H}$ are the global matrices corresponding to $\mathbf{Q}^e$ and $\mathbf{H}^e$, respectively, and $\mathbf{b}$, $\mathbf{s}$, and $\boldsymbol{\psi}$ are the global vectors corresponding to $\mathbf{b}^e$, $\mathbf{s}^e$ and $\boldsymbol{\psi}^e$, respectively. The bilinear constitutive equations (14b), when evaluated at node j, become

$$\{\tilde{\boldsymbol{\psi}}\}_j = \begin{cases} \{c^2\mathbf{s}\}_j, & \{c^2\mathbf{s}\}_j > -\{\mathbf{p}_{\mathrm{eq}}\}_j \\ -\{\mathbf{p}_{\mathrm{eq}}\}_j, & \{c^2\mathbf{s}\}_j \leqslant -\{\mathbf{p}_{\mathrm{eq}}\}_j \end{cases} \tag{29}$$

where $\mathbf{p}_{\mathrm{eq}}$ is a column vector of nodal equilibrium pressures.

The integrals in (27) are approximated with GLL quadrature. Since nodes and quadrature points are coincident, and because of (23), $\mathbf{Q}^e$ is diagonal, which facilitates use of the explicit time-integration scheme used here. For this study, the capacitance matrix is always formed and stored as a global diagonal matrix. In the explicit scheme (discussed below), most of the computation time is devoted to evaluation of the matrix–vector product $\mathbf{H}\boldsymbol{\psi}$, which must be evaluated at each time step. For Legendre-polynomial spectral elements, it is most efficient to evaluate the matrix–vector product element-by-element using *tensor-product factorizations* [41, 46, 59, 60], of which a detailed description may be found in Reference [61]. In addition to fast evaluation of the matrix–vector product, tensor-product factorization removes the memory requirements associated with storing $\mathbf{H}$ and/or $\mathbf{H}^e$, which can be demanding due to the high inter-element nodal coupling. We postpone discussing the formation of $\mathbf{b}^e$ until Section 2.2.5.

2.2.2. CASE: scattered-field model. We spatially discretize (15a) with the standard Galerkin approach as outlined in the previous section; the resulting scattered-field global CASE equations are

$$\mathbf{Q}\mathbf{s}_{\mathrm{sc}} + \mathbf{H}\boldsymbol{\psi}_{\mathrm{sc}} = \mathbf{b}_{\mathrm{sc}}$$

$$\{\tilde{\boldsymbol{\psi}}_{\mathrm{sc}}\}_j = \begin{cases} \{c^2\mathbf{s}_{\mathrm{sc}}\}_j, & \{c^2\mathbf{s}_{\mathrm{sc}}\}_j > -\{\mathbf{p}_{\mathrm{eq}} + \mathbf{p}_{\mathrm{inc}}\}_j \\ -\{\mathbf{p}_{\mathrm{eq}} + \mathbf{p}_{\mathrm{inc}}\}_j, & \{c^2\mathbf{s}_{\mathrm{sc}}\}_j \leqslant -\{\mathbf{p}_{\mathrm{eq}} + \mathbf{p}_{\mathrm{inc}}\}_j \end{cases} \tag{30}$$

where $\mathbf{Q}$ and $\mathbf{H}$ are formed as discussed in the previous section, $\mathbf{p}_{\mathrm{inc}}$ is a column vector of known nodal incident pressures, and the scattered boundary-interaction vector $\mathbf{b}_{\mathrm{sc}}$ is composed of element-level vectors defined by

$$\mathbf{b}_{\mathrm{sc}}^e = \int_{\Gamma^e} \boldsymbol{\phi}\nabla\psi_{\mathrm{sc}} \cdot \boldsymbol{n}\, \mathrm{d}\Gamma \tag{31}$$

Numerical implementation of the above scheme is identical to that discussed in the previous section.

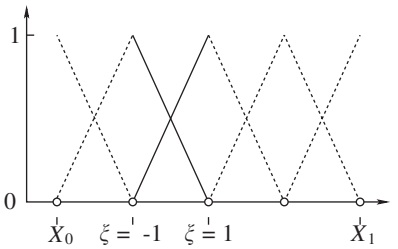

Figure 5. Basis functions for $N = 4$ CAFE refinement of a 1D element with endpoints at X_0 and X_1. The natural co-ordinates $(-1 \leqslant \xi \leqslant 1)$ pertain to the basis functions shown with the solid lines. This is the CAFE equivalent of Figure 4.

2.2.3. CAFE. We use the above CASE formulation to develop a CAFE formulation similar to that of Felippa and DeRuntz [7]. This is achieved by replacing the Lagrangian interpolants (21) with a series of bilinear functions, as illustrated in Figure 5 for a 1D element with endpoints at X_0 and X_1, and $N = 4$ CAFE refinement. This approach is equivalent to separating the original fluid element into multiple CAFEs. The basis functions and the natural co-ordinates for a single sub element are illustrated by the solid lines in Figure 5. Standard 8-point Gauss integration is used for evaluation of the 3D element-level matrices in (27), which produces a non-diagonal element-level capacitance matrix $\mathbf{Q}^e$; following Reference [7], we diagonalize $\mathbf{Q}^e$ with row-sum lumping. The semi-discrete equations appear identical to (28) and (30a) for the TFM and SFM, respectively.

Henceforth, we use N as a general refinement parameter. For CASE refinement, N denotes the polynomial order of the basis functions; for CAFE refinement, N denotes the number of element divisions applied to the base fluid element in each of the natural-co-ordinate directions. With either method, N refinement fills a base fluid element with $(N + 1)^3$ nodes.

As with the CASE model, the diagonal global capacitance matrix is formed and the most expensive part of evaluating the time-update equations lies in the evaluation of $\mathbf{H}\boldsymbol{\psi}$. However, unlike CASE, because of reduced nodal coupling and the absence of a tensor-product factorization, the most efficient method for evaluation is achieved with a global matrix–vector product. The matrix $\mathbf{H}$ for CAFE is created by forming the element-level matrices and storing them globally with a sparse-storage scheme in which only non-zero entries are stored.

2.2.4. Non-reflecting boundary and structure finite-elements. For this study, the non-reflecting boundary is the curved-wave approximation (CWA), which is an early-time approximation [62] in that it approaches exactness as $t \to 0$. More advanced non-reflecting boundaries may be used; Felippa and DeRuntz [7] truncated their CAFE mesh with a first-order DAA boundary. While the DAA is much better than CWA because it treats added-mass effects, it is expensive in terms of memory storage. In fact, a DAA is unnecessary, as an adequate CAFE or CASE mesh handles most of the added-mass effects. The specific CWA equations for the TFM and SFM may be found in Reference [61].

For the purposes of this study, the structural finite-element model is limited to 4-node, isoparametric, quadrilateral shell elements. The well-known semi-discrete FE equations for

linear, undamped structural motion (relative to equilibrium) at the element level are

$$\mathbf{M}^e\ddot{\mathbf{x}}^e + \mathbf{K}^e\mathbf{x}^e = \mathbf{f}^e \tag{32}$$

Here, $\mathbf{M}^e$ and $\mathbf{K}^e$ are the symmetric consistent-mass and stiffness matrices, respectively, and $\mathbf{x}^e$ and $\mathbf{f}^e$ are column vectors of nodal displacements and nodal forces, respectively.

For this study, the element-level matrices $\mathbf{M}^e$ and $\mathbf{K}^e$ are generated with ABAQUS [22]. For the shell elements, the fully integrated S4 quadrilateral element is used. This element has a consistent mass matrix, six degrees of freedom at each node, and accounts for membrane, bending and shear stiffness, as well as rotatory inertia. For the explicit time-integration scheme used here, evaluation of (32) is simplified and accuracy is improved with the use of a diagonal lumped-mass matrix, $\tilde{\mathbf{M}}^e$. For the shell elements, this is formed from $\mathbf{M}^e$ with an HRZ (Hinton, Rock and Zienkiewicz) lumping scheme [33].

2.2.5. FE/fluid-volume/non-reflecting-boundary coupling. With the above formulation, we have three separate semi-discrete models that interact at their interfaces: structure, fluid-volume and non-reflecting boundary. Displacements are output from the structure FE model and non-reflecting boundary to the fluid-volume mesh, from which pressures are returned [7]. This section discusses the specifics of numerical implementation for coupling of the three discrete models. Most importantly, a novel technique for coupling the fluid to the structure is introduced.

As discussed in the introduction, we wish to couple the structure and fluid models in a manner such that an arbitrary level of fluid refinement is allowed. To this end, we approach the problem as follows: (i) create a 'sufficiently refined' structure FE mesh composed of quadrilateral elements, (ii) create a base mesh for the fluid volume consisting of hexagonal elements whose quadrilateral faces are coincident with structure-element faces along the fluid–structure interface. With this approach, a coupling scheme may be constructed such that the base fluid mesh may be refined indefinitely with p (CASE) or h (CAFE) refinement without changing the structure mesh. This is illustrated in Figure 6 for $N = 4$ refinement, where we have maintained a one-to-one coupling between fluid and non-reflecting-boundary nodes.

With this method, the fluid and structure models are joined by a membrane composed of quadrilaterals. The fluid pressure may be numerically integrated over this surface and applied to the structure nodes. Likewise, the structure displacement at any point on the quadrilateral may be found by linear interpolation of the displacements at the corner points for output to the fluid mesh.

Structure forcing due to fluid response occurs as a pressure normal to the shell surface; there is no forcing on structure rotational DOF. The element-level structure-FE forcing vector $\mathbf{f}^e$ is assembled from three 4-component (4-node) vectors $\mathbf{f}^e_X$, $\mathbf{f}^e_Y$ and $\mathbf{f}^e_Z$, each corresponding to one of the three global Cartesian directions; again, the components of $\mathbf{f}^e$ for rotational DOF are zero. The vector for i-direction forcing is evaluated as

$$\mathbf{f}^e_i = \gamma^e_i \int_{\Gamma_{\text{wet}}} \mathbf{N}\bar{p}^e_{\text{dyn}}\,\mathrm{d}\Gamma \tag{33}$$

where $\mathbf{N}$ is a column vector of the standard bilinear shape functions [33], $\bar{p}^e_{\text{dyn}}$ is the *average* of the dynamic pressure $(p - p_{\text{eq}})$ over the element face, and γ^e_i is the cosine of the angle between the structure-element normal (positive going out of the fluid) and the ith global Cartesian direction. Numerical experiments comparing the use of $\bar{p}^e_{\text{dyn}}$ instead of $p^e_{\text{dyn}}(\xi, \eta)$

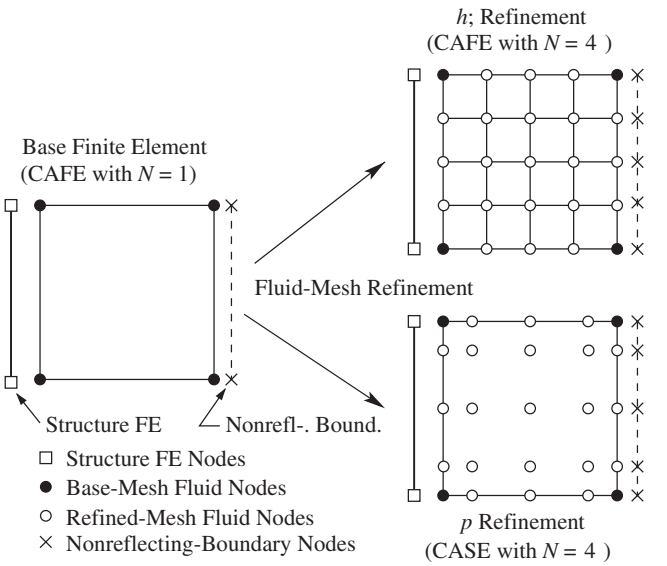

Figure 6. Fluid-refinement approaches and fluid–structure coupling, shown for a single hexagonal fluid element.

have been performed with ξ and η as the natural co-ordinates over the shell surface. For the cases studied, the use of the constant pressure yields more accurate structure responses as a result of reduced spurious ringing. A similar pressure-averaging approach for fluid–structure coupling has been successfully used for over 20 years in the USA code [63].

The fluid CAFE or CASE model is coupled at every boundary point to either a known-pressure boundary (free surface), a symmetry plane, a flexible structure or a non-reflecting boundary. At a known-pressure boundary, the boundary values are enforced in the time-update equations. At a symmetry plane, the normal fluid displacements must vanish, i.e. $-\rho_a \boldsymbol{\nabla}\psi \cdot \boldsymbol{n} = 0$, where $\boldsymbol{n}$ is the normal vector for the plane. As this is a natural boundary condition, ψ is left free along symmetry planes. Forcing at the structure/fluid and fluid/non-reflecting-boundary interfaces occurs through the boundary-interaction vector.

For the total-field fluid model, the boundary interaction vector (27c) is evaluated as

$$\mathbf{b}^e = -\rho_a \int_{\Gamma^e_{\mathrm{st}}} \boldsymbol{\phi} \bar{x}^e \, \mathrm{d}\Gamma - \rho_a \int_{\Gamma^e_{\mathrm{nrb}}} \boldsymbol{\phi}\boldsymbol{\phi}^{\mathrm{T}} (\mathbf{u}^e - \mathbf{u}^e_{\mathrm{eq}}) \, \mathrm{d}\Gamma \tag{34}$$

where $\bar{x}^e$ is the average normal structure displacement (positive going out of the fluid) at the centre of the wet-structure element, Γ^e_{st} is the quadrilateral area separating the wet-structure element from the fluid element, and Γ^e_{nrb} is the quadrilateral area of the non-reflecting boundary. The first integral in (34) is evaluated in closed form; the second is evaluated with GLL quadrature for CASE refinement and trapezoidal-rule integration for CAFE refinement.

For the scattered-field model, the boundary-interaction vector (31) is evaluated as

$$\mathbf{b}_{\mathrm{sc}}^{e} = -\rho_a \int_{\Gamma_{\mathrm{st}}} \boldsymbol{\phi} \bar{x}_{\mathrm{sc}}^{e} \, \mathrm{d}\Gamma - \rho_a \int_{\Gamma_{nrb}} \boldsymbol{\phi}\boldsymbol{\phi}^{\mathrm{T}} \mathbf{u}_{\mathrm{sc}}^{e} \, \mathrm{d}\Gamma \tag{35}$$

where $\bar{x}_{\mathrm{sc}}^{e}$ is the average *scattered* normal displacement (positive going into the fluid) at the centre of the wet-structure element; it is formed by subtracting the known incident displacement from each node's total displacement, projecting the resulting scattered displacement onto the normal of the element, and calculating the average over the element face.

2.3. Temporal discretization

2.3.1. Staggered integration with subcycling. The semi-discrete fluid and structure equations are both integrated with a conditionally stable explicit central-difference algorithm. Integration of the fluid and non-reflecting-boundary equations follow the method of Reference [7], where the fluid equations are integrated with numerical damping proportional to $\dot{s}$ in order to suppress frothing. Unlike the previous implementation, we incorporate structure and fluid time-step subcycling, which allows for efficient and accurate integration of the system equations. With subcycling, we allow both the fluid and structure to be integrated with time increments close to the maximum values allowed by their respective stability criteria. In the following, we give a qualitative description of our time-integration procedure; a detailed description may be found in Reference [61]. The implementation is the same for both CASE and CAFE.

We consider first subcycling of the structure equations so that $\Delta t_{\mathrm{fl}}/\Delta t = \alpha \geqslant 1$, where Δt_{fl} and Δt are the fluid and structure time increments, respectively. The time-update procedure for $\alpha = 2$ is illustrated in Figure 7(a). We assume that the state at all system nodes is known at time t (and at the previous time step) and we wish to update the values at all nodes to time $t + \alpha\Delta t$.

The surface-normal displacements at all nodes on the wet structure and on the non-reflecting boundary are predicted at time $t + \alpha\Delta t$ using a simple Euler scheme, i.e. $f(t + \Delta t) = f(t) + \Delta t \dot{f}(t)$ (step 1). These predicted values are denoted by the circled $\times$ and circled square. With these predicted values, the fluid equations are updated with central differences to $t = \alpha\Delta t = 2\Delta t$ (step 2). The updated fluid values are then used to correct the normal displacements of the non-reflecting-boundary nodes (step 3). With the fluid state known at $t + \alpha\Delta t$, the nodal pressures on the structure–fluid interface at $t + \Delta t$ are calculated by interpolation and the structure equations are updated with central differences (step 4). This is repeated until the state of all structure nodes is known at $t + \alpha\Delta t$ (step 5).

For $\alpha < 1$, the fluid equations are subcycled rather than those of the structure, as illustrated in Figure 7(b) for $\alpha = \frac{1}{2}$. This procedure is very similar to that for $\alpha \geqslant 1$, however, the structure state must be predicted for each fluid update.

2.3.2. Stability. Felippa and DeRuntz [7] performed a detailed stability analysis of integration with the FE/CAFE/non-reflecting-boundary approach; the structure model was integrated implicitly whereas the fluid model was integrated explicitly. Owing to the complexity of our system, we restrict ourselves to a stability analysis of the uncoupled fluid equations. We begin by assuming that we have a conservative estimate for the critical Δt for the structure and we use the results of Reference [7] for our stability analysis of the discrete fluid equations.

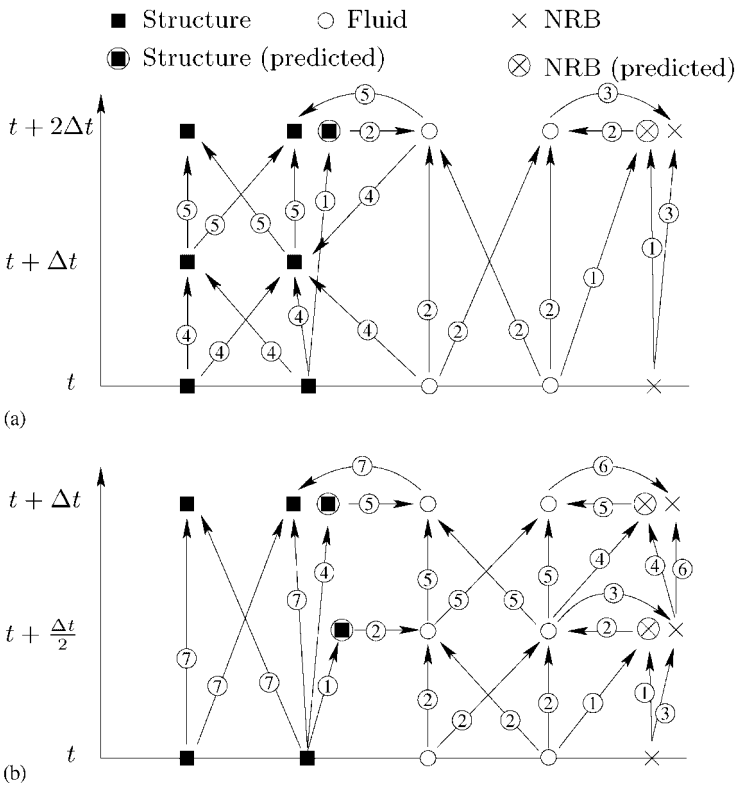

Figure 7. Information transfers for explicit-structure/explicit-fluid integration with: (a) structure subcycling ($\alpha = 2$); and (b) fluid subcycling ($\alpha = 1/2$). The circled numbers in (a) correspond to the step numbers discussed in the text, and Δt is the structure time increment.

For the fluid equations, an upper bound for the time increment is

$$\Delta t_{\text{cr}} = \frac{2}{c\sqrt{\lambda_{\max}(1 + 2\beta)}} \tag{36}$$

in which β is the artificial-damping constant and $\lambda_{\max}$ is the maximum eigenvalue of the global generalized eigenproblem

$$(\mathbf{H} - \lambda \mathbf{Q})\mathbf{z} = \mathbf{0} \tag{37}$$

The global $\lambda_{\max}$ may be bounded by the largest eigenvalue of the unassembled element-level matrices [33], i.e. $\lambda_{\max} = \max(\lambda^e_{\max})$, where $\lambda^e_{\max}$ is the maximum eigenvalue of the element-level eigenproblem

$$(\mathbf{H}^e - \lambda^e \mathbf{Q}^e)\mathbf{z}^e = \mathbf{0} \tag{38}$$

For the CAFE implementation, $\lambda_{\max}$ may be bounded above by $4/\Delta x^2_{\min}$ [7, 64] where $\Delta x_{\min}$ is the minimum distance between nodes in the fluid mesh. With this bound, the CAFE stability

limit may be written as

$$\Delta t_{\mathrm{cr}}^{\mathrm{cfl}} = \frac{\Delta t_{\mathrm{cfl}}}{\sqrt{1+2\beta}} \tag{39}$$

where $\Delta t_{\mathrm{cfl}} = \Delta x_{\min}/c$ is the Courant–Freidrichs–Lewy (CFL) [33] increment limit.

For CASE discretization, a simple upper-bound estimate on $\lambda_{\max}$ is not available. However, we may form the element-level matrices and use Gerschgorin's theorem to obtain an upper bound on $\lambda_{\max}$ [33, 65]. For the generalized Eigenproblem (38), Gerschgorin's theorem states that

$$\lambda_{\max}^{e} \leqslant \lambda_{\max}^{e,g} = \max\left[\left(H_{ii}^{e} + \sum_{j=1, j\neq i}^{(N+1)^3} |H_{ij}^{e}|\right) \Big/ Q_{ii}^{e}\right], \quad \forall i \in \{1, \ldots, (N+1)^3\} \tag{40}$$

where H_{ij}^{e} and Q_{ij}^{e} are elements of $\mathbf{H}^{e}$ and $\mathbf{Q}^{e}$, respectively, and $\mathbf{Q}^{e}$ is assumed diagonal. We define the Gerschgorin critical time increment for CASE as

$$\Delta t_{\mathrm{cr}}^{g} = \frac{2}{c\sqrt{\lambda_{\max}^{g}(1+2\beta)}} \tag{41}$$

where $\lambda_{\max}^{g} = \max(\lambda_{\max}^{e,g})$, $\forall e \in \{1, \ldots, n_{\mathrm{el}}\}$. We note that $\Delta t_{\mathrm{cr}}^{\mathrm{cfl}}$ does not require the formation of any matrices, whereas $\Delta t_{\mathrm{cr}}^{g}$ requires the formation of element-level matrices.

2.4. Error factors

In this section, we discuss a modified form of the Geers comprehensive error factor [32, 66], which may be used to quantify the error of transient response histories relative to an accepted benchmark solution. The comprehensive error (C-error) factor is given by $C = \sqrt{M^2 + P^2}$, in which $M = \sqrt{\vartheta_{cc}/\vartheta_{bb}} - 1$ and $P = \frac{1}{\pi}\arccos(\vartheta_{bc}/\sqrt{\vartheta_{bb}\vartheta_{cc}})$, where

$$\begin{aligned} \vartheta_{bb} &= (t_2 - t_1)^{-1} \int_{t_1}^{t_2} b^2(t)\,\mathrm{d}t, \quad \vartheta_{cc} = (t_2 - t_1)^{-1} \int_{t_1}^{t_2} c^2(t)\,\mathrm{d}t \\ \vartheta_{bc} &= (t_2 - t_1)^{-1} \int_{t_1}^{t_2} b(t)c(t)\,\mathrm{d}t \end{aligned} \tag{42}$$

In these equations, $c(t)$ is a candidate solution in the form of a response history, $b(t)$ is the corresponding benchmark history, and $t_1 \leqslant t \leqslant t_2$ is the time span of interest. M is the *magnitude error factor*, which is insensitive to phase discrepancies, and P is the *phase error factor*, which is insensitive to magnitude discrepancies. In earlier applications, the phase error factor was given by $\tilde{P} = 1 - \vartheta_{bc}/\sqrt{\vartheta_{bb}\vartheta_{cc}}$, which we have found to be insufficiently sensitive to phase errors.

3. 1D EVALUATION: 2-DOF FLOATING MASS–SPRING OSCILLATOR

3.1. Problem description

For initial evaluation of CASE, field separation, and non-conformal fluid–structure coupling, we use a benchmark model consisting of a semi-infinite, 1D fluid column that supports a

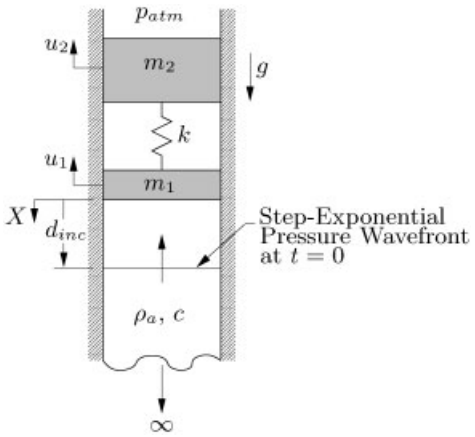

Figure 8. Physical model used to represent a ship for the 1D benchmark problem; the lower mass represents the ship's hull and the upper mass its internal structure and equipment.

2-degree-of-freedom (2DOF) mass–spring oscillator; the lower mass represents the ship's hull and the upper mass its internal structure and equipment. This model was productively employed in a recent evaluation of field separation and a 1D CASE implementation [32].

The benchmark model mentioned above is shown in Figure 8. The hull mass is m_1 and the total mass of internal structure and equipment is m_2. The masses are separated by a linear spring with stiffness k and the fluid column has cross-sectional area a. The displacements of m_1 and m_2 are $u_1(t)$ and $u_2(t)$, respectively. Depth relative to the equilibrium position of the wet surface of m_1 is denoted by X, and g is the acceleration of gravity.

The incident field driving the hull mass is due to a plane, upward propagating, step-exponential acoustic wave defined by

$$p_{\text{inc}}(X,t) = p_0 \exp\left[-\frac{t + (X - d_{\text{inc}})/c}{\tau}\right] H[t + (X - d_{\text{inc}})/c] \tag{43}$$

where p_0 and τ are the peak pressure and decay time, respectively, and $H()$ is the Heaviside step function. At $t = 0$, the incident wavefront is located at a standoff d_{inc} from the wet surface of m_1.

The physical properties used in the 1D calculations are $\rho_a = 1026\,\text{kg/m}^3$, $c = 1500\,\text{m/s}$, $p_{\text{atm}} = 0.101\,\text{MPa}$, $g = 9.81\,\text{m/s}^2$, and $a = (0.3\,\text{m})^2$. For the ship model, $m_2/m_1 = 5$ and $m_1 = 76.9\,\text{kg}$, which produce an equilibrium draft for the corresponding 3D structure of 5 m. The spring stiffness k is such that the fixed-base natural frequency of m_2 is 5 Hz. The incident wave corresponds to the shock wave generated by a 45.4 kg charge of HBX-1 detonated at a 10 m standoff from the wet surface of the hull mass, so that $p_0 = 16.2\,\text{MPa}$ and $\tau = 0.42\,\text{ms}$ [67].

3.2. Discrete model and benchmark solution

The upper and lower structure masses are represented by square 4-node structural plate finite-elements with cross-sectional area equal to $(0.3\,\text{m})^2$. The base fluid mesh ($N = 1$ refinement)

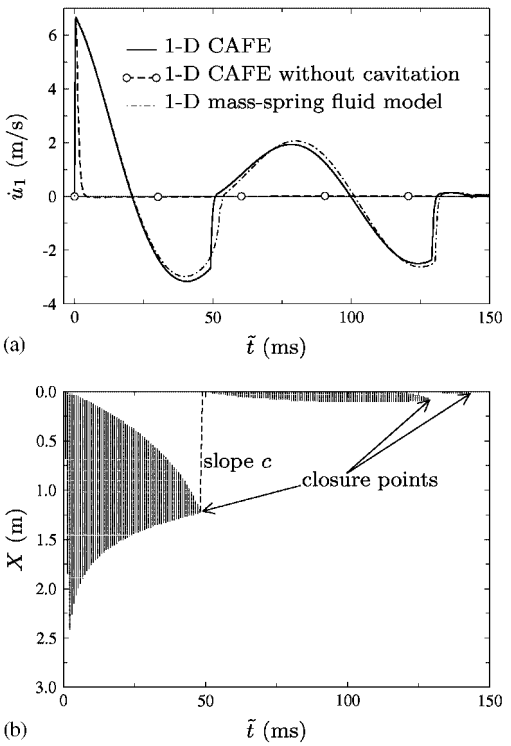

Figure 9. (a) Benchmark velocity histories of m_1 produced with a 1D CAFE model [13] and a 1D Lagrangian spring–mass model; and (b) the associated space–time cavitation zones produced with the CAFE model. The dashed line in (b) denotes a fluid characteristic, which relates the pressure pulse caused by cavitation closure to the associated change in structure velocity.

is composed of 10 cube elements with 0.3 m sides. The fluid mesh is terminated by a plane-wave-approximation boundary element located at $d_{\mathrm{pw}} = 3\,\mathrm{m}$, which is exact for 1D waves. The CAFE and CASE models are integrated without subcycling ($\alpha = 1$) and with $\Delta t = 0.75\Delta t_{\mathrm{cr}}^{\mathrm{cfl}}$ and $\Delta t = \Delta t_{\mathrm{cr}}^{g}$, respectively. The artificial-damping coefficient $\beta = 0.25$. Time-step subcycling is not used because the critical time increment for the structure was too large for accurate solutions. At $t = 0$, the incident wavefront is located one base fluid element from the wet surface of m_1 ($d_{\mathrm{inc}} = 0.3$ m).

The benchmark results are the product of a 1D CAFE research code, which has been validated [13] with the benchmark problem of Bleich and Sandler [2]. The super-refined benchmark CAFE mesh has 24 000 equal-length elements and employs a mesh with $d_{\mathrm{pw}} = 3\,\mathrm{m}$, which lies below the 2.5 m maximum depth of cavitation [13].

The benchmark velocity responses of m_1 calculated with and without cavitation are shown in Figure 9(a) as a function of the delayed time $\tilde{t} = t - d_{\mathrm{inc}}/c$. Also, shown are the results produced with a Lagrangian mass–spring model of the fluid, which is discussed below. Clearly, cavitation has a profound effect on the structure response. Figure 9(b) shows the associated space–time cavitation zones; the grey areas indicate the existence of cavitation, where and

when absolute pressure is zero. We note that the abrupt changes in $\dot{u}_1$ at $\tilde{t} = 49$ ms and $\tilde{t} = 129$ ms are due to pressure pulses caused by *closure* of the initial two cavitation regions (see Figure 9(b)). The closure of the third, and smallest, cavitation region causes a small kink in $\dot{u}_1$ at $\tilde{t} = 144$ ms.

When deriving the linearized governing equations (14), we assumed that the condensation was small and that the convective term in the momentum equation was negligible. In order to test these assumptions, we now repeat the analysis of the above problem, but represent the fluid with a discrete system of springs and masses. Hence, this model employs a Lagrangian treatment of motion, in which the dynamic pressure between two fluid masses m_i and m_j is given by

$$p_{ij} = \begin{cases} B_a \dfrac{\varepsilon_{ij}}{1 + \varepsilon_{ij}}, & p_{ij} \geqslant p_{\text{eq}} \\ -p_{\text{eq}}, & p_{ij} < p_{\text{eq}} \end{cases} \tag{44}$$

Here, $\varepsilon_{ij} = (u_i - u_j)/\Delta X$, where u_i is the dynamic displacement of m_i, and ΔX is the equilibrium separation of m_i and m_j. As with the benchmark CAFE model, the system is bounded by a plane-wave boundary at $d_{\text{pw}} = 3$ m, and the semi-discrete equations are integrated in time with a central-difference algorithm and $\dot{s}$-proportional damping.

As mentioned above, Figure 9(a) shows the m_1 velocity histories calculated with the CAFE benchmark model and a highly refined spring–mass fluid model (20 000 DOF). The agreement is seen to be quite good ($C = 0.040$), where the differences may be attributed to the neglected terms in the CAFE governing equations. The discrepancy between the response histories is too small to justify the expense associated with a hydrocode that treats the neglected terms. With cavitation effects neglected, the two models produce response histories that are indistinguishable from one another.

3.3. Results and discussion

Using the base fluid model discussed above, we examined the performance of CAFE refinement with the scattered-field model (CAFE-SFM) and CASE refinement with both the scattered-field model (CASE-SFM) and with the total-field model (CASE-TFM). In particular, we calculated C-errors for m_1 velocity-response histories (relative to the benchmark solution discussed above) as a function of fluid DOF, memory storage and operations. Memory-storage and operation requirements pertained to storage and evaluation of the matrix–vector product $\mathbf{H}\boldsymbol{\psi}$, which must be evaluated for each time step and is the most expensive component of time integration.

The conclusions drawn from this study agree with those reached in the performance study of our 1D CAFE and CASE implementations [32]. Because of this, we discuss the conclusions but do not show numerical results, which may be found in Reference [61]. For a given level of accuracy, CASE offers significant savings over CAFE in terms of fluid DOF and required memory; operation requirements were similar. Further, CASE produces greater gains in accuracy than CAFE for the same increase in spatial refinement. Also, although the scattered-field model degrades CASE performance for coarse meshes, it produces solutions with accuracy equivalent to those produced with the total-field model for refined meshes. Finally, the non-conformal coupling approach provides significant savings in the structure FE model, as no refinement is required to accommodate fluid-model refinement.

4. 3D EVALUATION: SUBMERGED SPHERICAL SHELL

In the previous section, a 1D problem was used to test the performance of CAFE-SFM, CASE-SFM, CASE-TFM, and non-conformal fluid–structure coupling. In this chapter, we extend the analysis to 3D by investigating the axisymmetric response of an empty, submerged spherical shell excited by an incident step-exponential spherical wave. Time-increment restrictions for the structure model also allow us to validate the use of time-step subcycling.

4.1. Problem description

A schematic of the spherical shell and incident wave is shown in Figure 10. The fluid is infinite and homogeneous and gravity is neglected. The shell has thickness h, mid-surface radius a, Young's modulus E, density ρ_s and Poisson's ratio v. Meridional and radial displacements are denoted by v and w, respectively. Cartesian (X, Y) and spherical (r, θ) co-ordinate frames are shown. The incident-wave centre is located at $\boldsymbol{X}_c = (X_c, Y_c, Z_c)$, and the pressure field is defined by

$$p_{\text{inc}}(\boldsymbol{X}, t) = \frac{R_0}{R} p_0 \exp\left[-\frac{t - (R - R_0)/c}{\tau}\right] H[t - (R - R_0)/c] \tag{45}$$

where $R = |\boldsymbol{X} - \boldsymbol{X}_c|$, and the wavefront has radius R_0 and peak pressure p_0 when $t = 0$. As in the 1D problem, d_{inc} is the wavefront standoff from the structure when $t = 0$. The physical parameters used in this analysis are listed in Table I. The incident-wave peak pressure and decay time correspond to a 60 kg charge of HBX-1 [5, 6] detonated at a 12 m standoff. The uniform hydrostatic pressure corresponds to a depth of 50 m.

4.2. Discrete model, validation and benchmark solution

4.2.1. Discrete models. Since this problem is axisymmetric, we use quarter-symmetry models that reduce computational cost but retain the complexity of the 3D system. Figure 11 shows

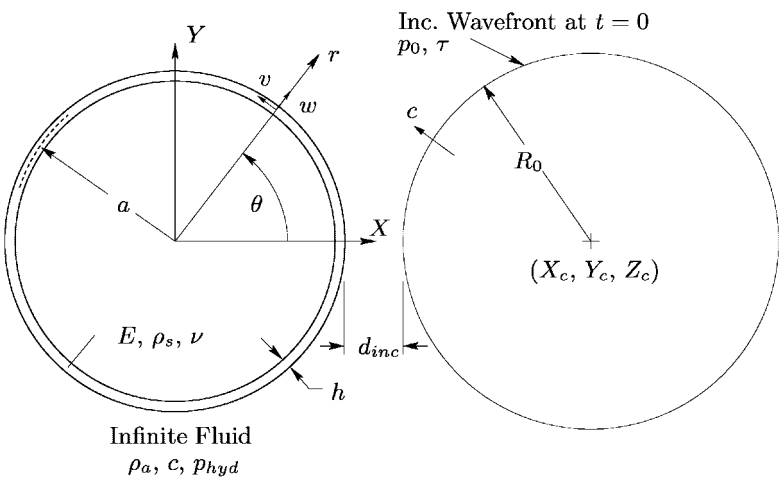

Figure 10. Schematic of the spherical shell and incident spherical wave with associated variables.

Table I. Properties used for the spherical shell, water and incident wave.

Young's modulus	E	195×10^9 Pa
Shell density	ρ_s	7700 kg/m^3
Poisson's ratio	ν	0.3
Shell radius	a	5 m
Shell thickness	h	0.05 m
Water density	ρ_a	1026 kg/m^3
Water sound speed	c	1500 m/s
Hydrostatic pressure	p_{hyd}	0.604 MPa
Inc.-wave peak press	p_0	16.26 MPa
Inc.-wave decay time	τ	0.464 ms
Inc.-wave centre	$X_c,\ Y_c,\ Z_c$	(17, 0, 0) m

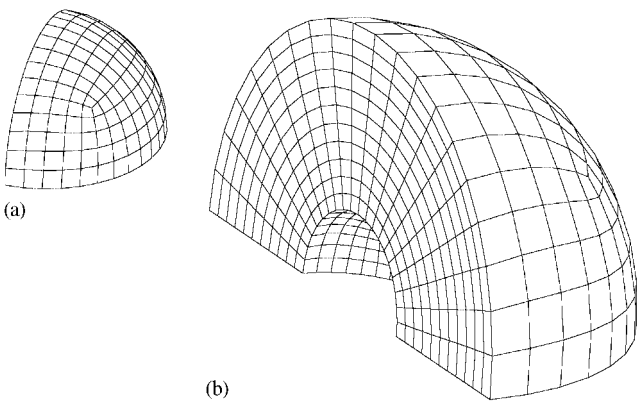

Figure 11. Quarter-symmetry discrete models used in the response calculations for a submerged spherical shell: (a) 150-element structure finite-element model; and (b) 1650-element base fluid mesh.

(a) the structure FE model and (b) the base fluid mesh that surrounds it. The structure mesh is composed of 150 quadrilateral elements, which was shown in Reference [61] to be sufficiently refined for the current problem. The fluid mesh is composed of 1650 hexagonal elements, has an outside radius of 15 m, and is surrounded by CWA elements.

4.2.2. Validation without cavitation. With cavitation effects neglected, this problem has been solved with modal methods for plane-step-wave excitation by Zhang and Geers [68]; their solution method has been incorporated into SPHSHK/MODSUM [69], a public-domain FORTRAN program. The program has been extended by Sprague and Geers [70] to include spherical and plane step-exponential incident waves. We use results produced with SPHSHK/MODSUM to validate our approach in the absence of cavitation.

For validation, subcycling and the scattered-field model were employed. Figure 12 shows non-dimensional structure radial-velocity response histories at $\theta = 0°$ and 180° as a function of non-dimensional delayed time. The responses were calculated with the 1650-element base fluid model and either $N = 10$ (1.7×10^6 DOF) or $N = 14$ (4.6×10^6 DOF) CASE refinement with

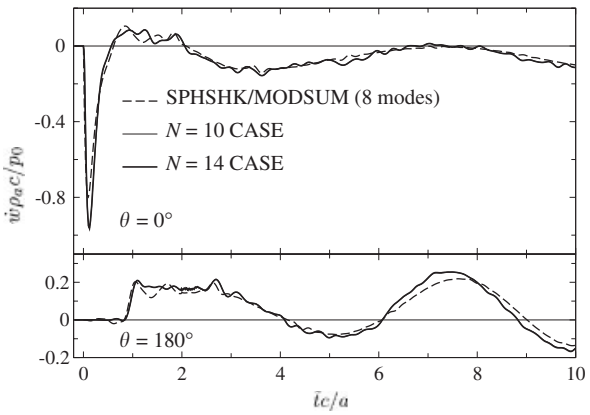

Figure 12. Non-dimensional spherical-shell radial-velocity histories calculated with two super-refined CASE fluid meshes coupled to the 150-element structure model. Cavitation effects are neglected. Also shown are the modal solutions produced by SPHSHK/MODSUM [69, 70]. The C-error values for the $N = 10$ solutions relative to the $N = 14$ solutions are $C = 0.003$ and 0.006 for $\theta = 0°$ and 180°, respectively.

$\alpha = \frac{1}{5}$ or $\alpha = \frac{1}{9}$, respectively ($\Delta t_{\mathrm{fl}} = \alpha \Delta t$). For this and subsequent calculations, the structure was integrated with $\Delta t = 7.5 \times 10^{-6}$ s and the incident wave was located a single base element from the structure at $t = 0$ ($d_{\mathrm{inc}} = 0.909$ m). Again, $\beta = 0.25$ was used. Also, shown are the response histories produced by SPHSHK/MODSUM with the first 8 modes. Differences between the two CASE solutions are indiscernible, which indicates convergence in terms of both spatial and temporal refinement. In addition, good agreement is seen between the CASE and modal solutions except at late time for $\theta = 180°$. These differences may be attributed to differences between the two structure formulations (the modal model neglects rotatory inertia and shear stiffness). These results serve to validate the implementation of CASE, fluid–structure coupling, and time-step subcycling. Solutions produced with CAFE appear identical to those shown for CASE for $N = 10$ and 14 refinement. We remark that in order to achieve a fluid-refinement level equivalent to the $N = 14$ model with the original one-to-one CAFE-FE coupling approach, the structure model would require $150N^2 = 29\,400$ elements.

4.2.3. Benchmark solution with cavitation. Having validated CAFE, CASE, subcycling and our fluid–structure coupling, we investigate the performance of the proposed method applied to the submerged shell, but in the presence of cavitation. In the absence of benchmark solutions for 3D FSI problems with cavitation, we use a super-refined CASE-SFM model to generate a benchmark solution. We use CASE-SFM because of its superiority demonstrated in the 1D test problem.

Figure 13 shows response histories for the front and back of the shell, as produced by CASE-SFM, subcycling, and either $N = 10$ or 14 refinement with $\beta = 0.25$. The response histories produced with $N = 10$ and 14 are virtually indistinguishable, thus indicating a converged solution. Further, it was found that the differences between response histories produced with $N = 14$ and either $\beta = 0.1$ and 0.25 were indistinguishable. Also, shown are the validation solutions for the non-cavitating system. Cavitation has a strong effect on the late-time response

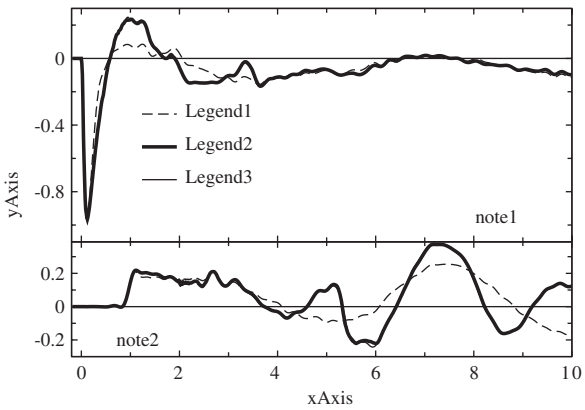

Figure 13. Non-dimensional spherical-shell radial-velocity histories calculated with two super-refined CASE-SFM fluid models coupled to the 150-element structure model. The hydrostatic pressure corresponds to a 50 m depth, and cavitation effects are included. Also, shown are the benchmark responses from Figure 12, which were calculated with cavitation effects neglected. The C-error values for the $N = 10$ solutions relative to the $N = 14$ solutions are $C = 0.009$ and 0.015 for $\theta = 0°$ and $180°$, respectively.

at the back of the shell but only a modest effect on early-time responses at the front of the shell.

Figures 14 and 15 show cavitation snapshots of the axisymmetric plane at various non-dimensional times. After the initial impact of the incident wave on the structure, the flexible shell behaves in a manner similar to a free surface; this behaviour causes the early-time formation of the cavitation region seen at the front of the shell. We see that cavitation also occurs at the shell's back side. While the size of this cavitation region shrinks rapidly, a small region of cavitation remains 'attached' to the back side of the shell for $2 < \tilde{t}c/a < 10$. It is this cavitation that causes the large late-time oscillations.

4.3. Results and discussion

In this section, we compare the performance of CAFE and CASE models with many fewer fluid DOF than the number used in the benchmark model. Table II shows the fluid DOF and subcycling ratios used for each refinement level. The subcycling ratios are based on $\Delta t = 7.5 \times 10^{-6}$ s, and were chosen such that $\alpha\Delta t$ was less than 75% $\Delta t_{\mathrm{cr}}^{\mathrm{cfl}}$ for CAFE and less than $\Delta t_{\mathrm{cr}}^{g}$ for CASE. We see that, because most of the ratios are quite different than one, subcycling offers significant computational savings. We note that the fluid time increment ($\alpha\Delta t$) is reduced more rapidly with CASE than CAFE with fluid refinement, thus offering more aggressive temporal refinement with spatial refinement.

Figure 16 shows radial-velocity response histories at the front and back of the shell calculated with CAFE-SFM or CASE-SFM and $N = 1, 2$ or 3 refinement. The solutions produced by both methods appear to be converging to the benchmark solutions with increasing refinement. Further, we see that CASE consistently outperforms CAFE and that CAFE fails to produce a response at $\theta = 180°$ with $C < 0.1$. CASE, however, requires $N = 3$ refinement to produce response histories at the two positions with $C < 0.1$. It is interesting to note the appearance

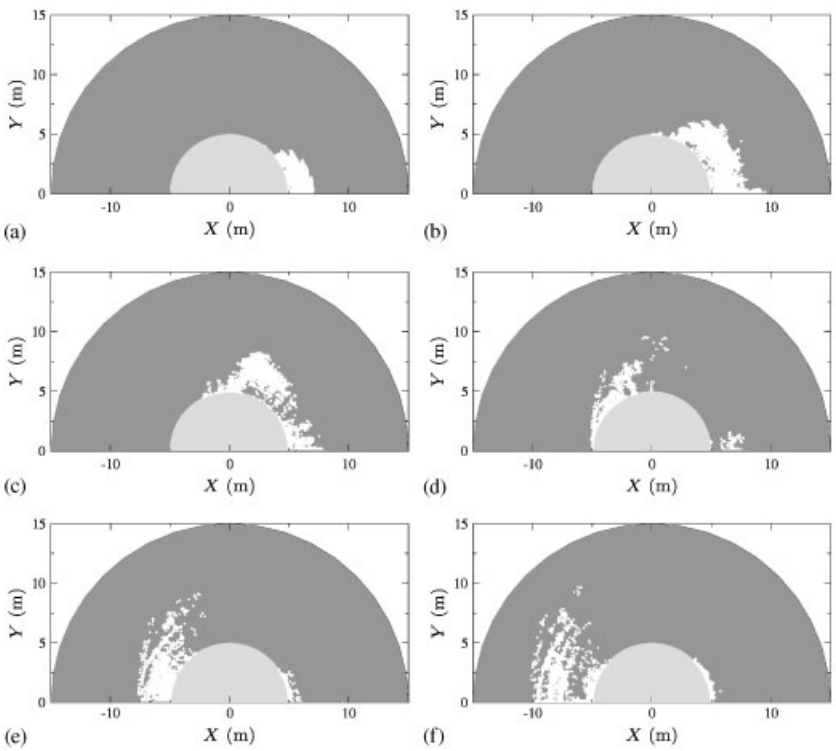

Figure 14. Axisymmetric cavitation snapshots for a spherical shell at a depth of 50 m for $0.5 \leqslant \tilde{t}c/a \leqslant 3.0$. Light grey represents the shell, dark grey represents the uncavitated fluid and white represents cavitated fluid. Results are a product of a CASE-SFM model with $N = 14$: (a) $\tilde{t}c/a = 0.5$; (b) $\tilde{t}c/a = 1.0$; (c) $\tilde{t}c/a = 1.5$; (d) $\tilde{t}c/a = 2.0$; (e) $\tilde{t}c/a = 2.5$; and (f) $\tilde{t}c/a = 3.0$.

of the abrupt oscillations at $\tilde{t}c/a = 2$ for the response histories at $\theta = 180°$. This is due to the fluid mesh's inability to capture the discontinuous scattered field associated with the arrival of the discontinuous incident wave. The magnitude of the oscillations decreases rapidly with increasing fluid-mesh refinement, however.

Figures 17–19 compare the performance of CAFE-SFM, CASE-SFM and CASE-TFM in terms of required fluid DOF, operations and memory, respectively. Here, we look at refinement levels that are well beyond those expected in practice in order to examine the convergence rates and overall performance of the methods.

In terms of required fluid DOF (Figure 17) for a given accuracy level, CASE-SFM appears to be the best choice. CAFE-SFM exhibits very slow convergence at $\theta = 180°$ and CASE-TFM performs consistently worse than CASE-SFM. At $\theta = 0°$, CAFE-SFM requires about 1.6 times the number of fluid DOF required by CASE-SFM to produce $C \approx 0.1$. At $\theta = 180°$, if one neglects the serendipitous 'dip' in CASE-SFM error at 1.5×10^4 fluid DOF, CAFE-SFM requires about 36 times the fluid DOF required by CASE-SFM to produce $C \approx 0.1$. In terms of required operations (Figure 18), CAFE-SFM slightly outperforms CASE-SFM for $\theta = 0°$, but produces unacceptable convergence at $\theta = 180°$. Finally, in terms of required memory

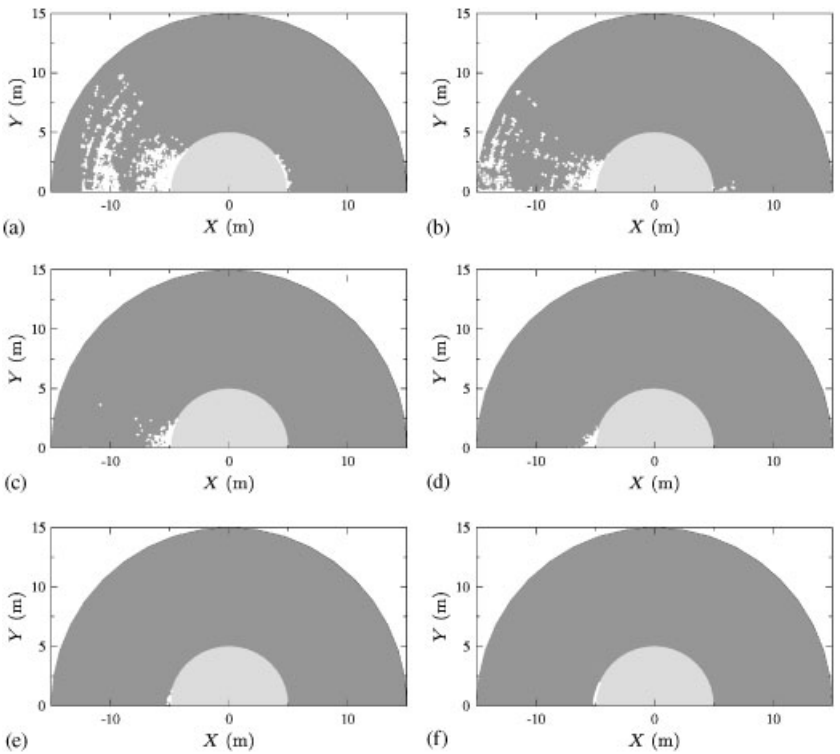

Figure 15. Axisymmetric cavitation snapshots for a spherical shell at a depth of 50 m for $3.5 \leqslant \tilde{t}c/a \leqslant 8$. Light grey represents the shell, dark grey represents the uncavitated fluid and white represents cavitated fluid. Results are a product of a CASE-SFM model with $N = 14$. The cavitation snapshots for $8 \leqslant \tilde{t}c/a \leqslant 10$ appear very similar to that in (f): (a) $\tilde{t}c/a = 3.5$; (b) $\tilde{t}c/a = 4.0$; (c) $\tilde{t}c/a = 4.5$; (d) $\tilde{t}c/a = 5.0$; (e) $\tilde{t}c/a = 5.5$; and (f) $\tilde{t}c/a = 8.0$.

Table II. Fluid-model properties for CAFE and CASE refinement of the 1650-element base fluid mesh shown in Figure 11(b).

N	Fluid DOF	CAFE α	CASE α
1	2052	20	14
2	14 743	10	4
3	47 974	6	2
4	111 645	5	2
5	215 656	4	1/2
6	369 907	3	1/2
8	868 729	2	1/3
10	1 687 311	2	1/5
14	4 600 555	1	1/9

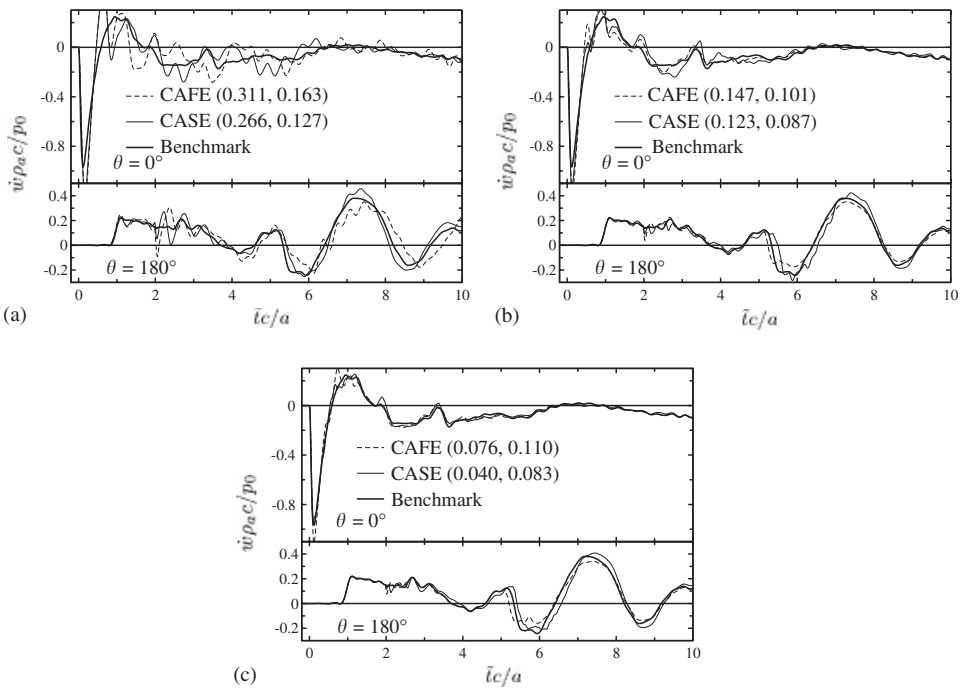

Figure 16. Non-dimensional radial-velocity histories for the spherical shell calculated with the either CAFE or CASE and the SFM. The benchmark solutions are the product of a CASE-SFM model with $N = 14$. The numbers in parentheses are the C-error values associated with the response histories at $\theta = 0°$ and 180°, respectively: (a) $N = 1$: 2052 fluid DOF; (b) $N = 2$: 14 743 fluid DOF; and (c) $N = 3$: 47 974 fluid DOF.

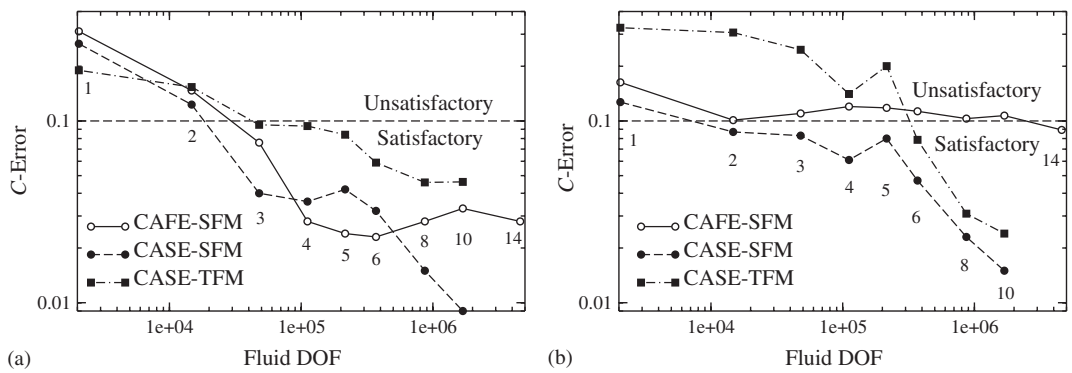

Figure 17. C-error values as a function of total fluid DOF for radial-velocity histories produced at the (a) front and (b) back of the spherical shell. Benchmark results were produced with an $N = 14$ CASE-SFM model: (a) $\theta = 0°$; and (b) $\theta = 180°$.

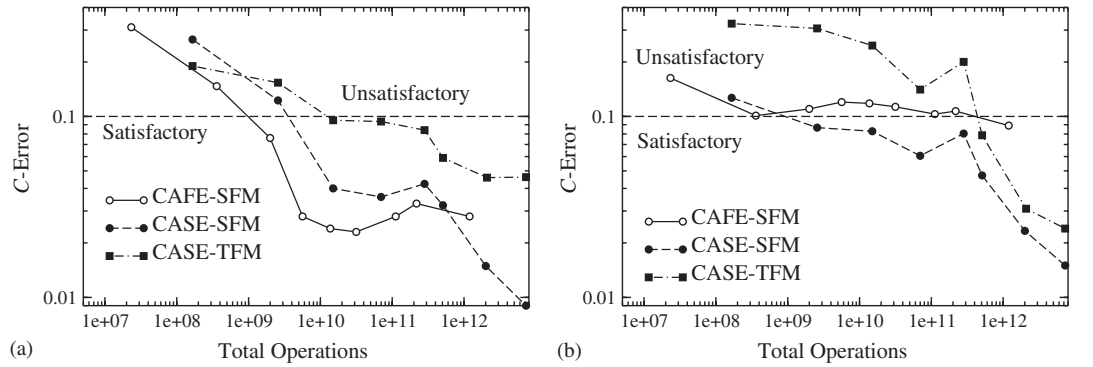

Figure 18. C-error values as a function of total operations required to evaluate the matrix–vector product $\mathbf{H}\boldsymbol{\psi}$ for radial-velocity histories produced at the (a) front and (b) back of the spherical shell. Benchmark results were produced with an $N = 14$ CASE-SFM model: (a) $\theta = 0°$; and (b) $\theta = 180°$.

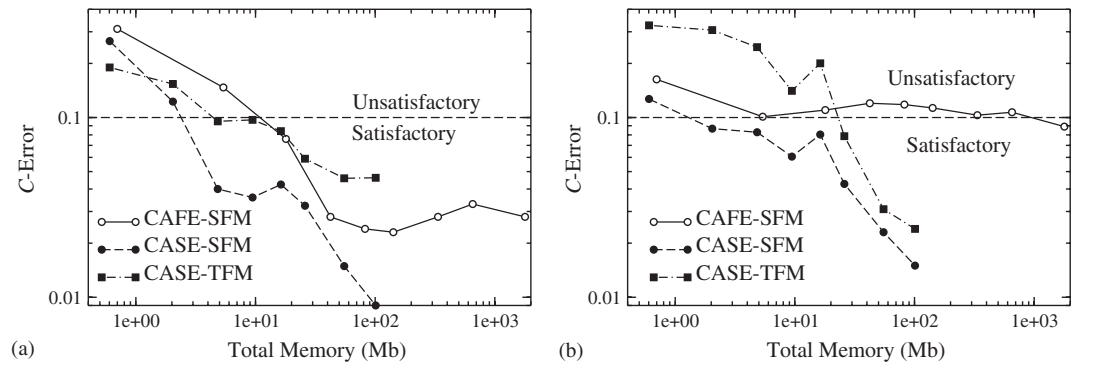

Figure 19. C-error values as a function of total memory storage required to evaluate the matrix–vector product $\mathbf{H}\boldsymbol{\psi}$ for radial-velocity histories produced at the (a) front and (b) back of the spherical shell. Benchmark results were produced with an $N = 14$ CASE-SFM model: (a) $\theta = 0°$; and (b) $\theta = 180°$.

(Figure 19), CASE-SFM is the clear winner. Although these results are not monotonically converging with refinement like the results for the 1D problem, they do follow the same trends. Overall, CASE-SFM exhibits the strongest convergence rates, and offers the greatest efficiency at a given refinement level.

In the above results, CASE-SFM significantly outperformed CASE-TFM for all but the coarsest mesh. As discussed earlier, we attribute the poor performance of TFM to distortion of the incident field. This distortion is caused by the inherent dispersion associated with the discrete fluid mesh and, less obviously, by spurious cavitation. Figure 20 shows cavitation snapshots for $\tilde{t}c/a = 1$. The results are the product of an $N = 6$ CASE model with either the TFM or SFM. For the TFM (Figure 20(a)), we see extensive frothing throughout the fluid domain in front of the shell, which is due to the passage of the incident wavefront. In the

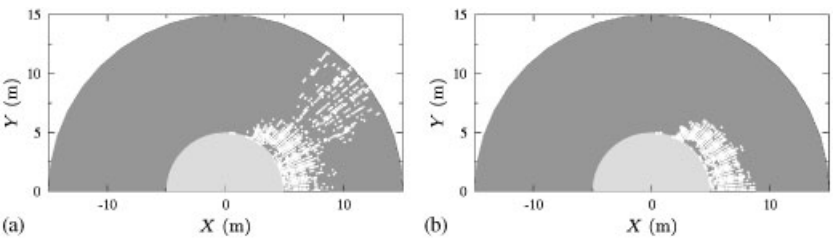

Figure 20. Axisymmetric cavitation snapshots for a spherical shell at a depth of 50 m at $\tilde{t}c/a = 1.0$. Results are a product of an $N = 6$ CASE model with the (a) TFM and (b) SFM.

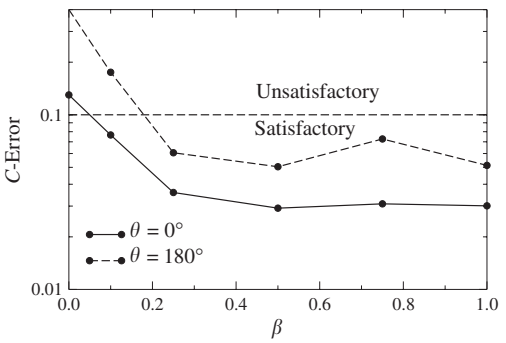

Figure 21. C-error values as a function of the artificial-damping parameter β for radial-velocity histories produced with CASE-SFM and $N = 4$ at the front and back of the spherical shell. Benchmark results were produced with an $N = 14$ CASE-SFM model.

CASE-TFM model, pressure oscillations that reach the cavitation threshold are produced by the mesh attempting to simulate the discontinuous incident field. This is not seen in the SFM model. Thus, frothing degrades incident-wave propagation and impedes model performance.

In the preceding test cases, the artificial-damping parameter was $\beta = 0.25$. Here, we examine the sensitivity of CASE-SFM responses to changes in β. Figure 21 shows the C-error of shell response histories calculated with CASE-SFM, $N = 4$ refinement, and various levels of damping. The performance of CASE-SFM is largely unaffected by changes in β for $0.25 < \beta < 1.0$. For $\beta < 0.25$, the error grows sharply with decreasing β. These results serve to support our choice of $\beta = 0.25$ in the preceding simulations.

For the sake of brevity, we have omitted several of the results found in Reference [61], but we mention here the findings obtained. First, for the submerged spherical shell, the advantages of CASE over CAFE are enhanced when cavitation is absent. Second, regarding Gauss quadrature for evaluation of the element-level integrals for CAFE matrices, full integration (8 point) should be used for hexagonal elements, as 1-point integration yields significantly poorer accuracy. Finally, the use of CASE and CAFE *without* the use of time-step subcycling not only required more operations, but significantly reduced accuracy.

5. SUMMARY AND CONCLUSIONS

In this paper, we introduced four improvements to the original cavitating acoustic finite-element (CAFE) approach for treating fluid cavitation in underwater-shock computations. These improvements are: (i) incorporation of field separation, (ii) replacement of CAFE with cavitating acoustic spectral elements (CASE), (iii) introduction of a new non-conformal structure–fluid coupling method and (iv) utilization of time-step subcycling. The improvements are independent of one another, thus allowing utilization of all or some in current finite-element software.

The efficiency of the improvements was examined by means of two canonical problems: (i) a 2-DOF floating mass–spring oscillator excited by a plane, step-exponential wave and (ii) a submerged spherical shell excited by a spherical, step-exponential wave. Both problems were examined with and without cavitation. The conclusions reached are as follows:

- *Field separation*: Separation of the total field into equilibrium, incident and scattered fields, i.e. the use of an SFM, is appealing because it allows accurate propagation of the incident field and admits realistic, quasi-acoustic shock fields. For the 1D problem, TFM and SFM exhibited similar performance. For the 3D problem, SFM considerably outperformed TFM, thereby allowing substantial reduction in the required number of fluid DOF.
- *Cavitating acoustic spectral elements*: For the 1D problem, CASE offered significant savings in required fluid DOF and memory storage relative to CAFE; moderate savings were seen in terms of required operations. The superiority of CASE was also seen in the 3D problem, but the savings were not as significant. Overall, CASE is a clear choice over CAFE due to comparable operation requirements, much smaller memory requirements and ease of parallelization. The CAFE implementation used here, which requires many fewer operations than an element-by-element formulation, is cumbersome due to the global sparse-storage scheme. CAFE can be efficiently implemented at the element level only if reduced integration is used. However, reduced integration degrades the method's accuracy to an unacceptable level.
- *Non-conformal fluid–structure coupling*: The use of non-conformal coupling greatly reduced the computational effort required to treat the structure. With satisfactory refinement in the structure, a converged fluid model was found without further structure refinement. Further, the coupling method is very simple in terms of implementation.
- *Time-step subcycling*: With subcycling, the structure and fluid may be integrated with near-optimal time increments. For the problems investigated, time-step subcycling offered large gains in accuracy for a given number of operations.

ACKNOWLEDGEMENTS

This research was funded by the Office of Naval Research under Grant N00014-01-1-0154, with support contributions made by the Naval Surface Warfare Center, Carderock Division.

REFERENCES

1. Kennard EH. Cavitation in an elastic liquid. *Physical Review* 1943; **63**(5/6):172–181.
2. Bleich HH, Sandler IS. Interaction between structures and bilinear fluids. *International Journal of Solids and Structures* 1970; **6**:617–639.

3. Driels MR. The effect of a non-zero cavitation tension on the damage sustained by a target plate subject to an underwater explosion. *Journal of Sound and Vibration* 1980; **73**(4):533–545.
4. Costanzo FA, Gordon JD. An analysis of bulk cavitation in deep water. *DTNSRDC*, *UERD Report*, May 1980.
5. Cole RH. *Underwater Explosions*. Princeton University Press: Princeton, NJ, 1948.
6. Price RS. Similitude equations for explosives fired underwater. *Technical Report* NSWC TR 80-299, NSWC, November 1979.
7. Felippa CA, DeRuntz JA. Finite element analysis of shock-induced hull cavitation. *Computer Methods in Applied Mechanics and Engineering* 1984; **44**:297–337.
8. Newton RE. Effects of cavitation on underwater shock loading—axisymmetric geometry. *Technical Report* NPS-69-78-017PR, Naval Postgraduate School, Monterey, CA, 1978.
9. Newton RE. Effects of cavitation on underwater shock loading—part 1. *Technical Report* NPS-69-78-013, Naval Postgraduate School, Monterey, CA, 1978.
10. Newton RE. Finite element analysis of shock-induced cavitation, 1980. ASCE Spring Convention, preprint 80-110.
11. Newton RE. Effects of cavitation on underwater shock loading—plane problem. *Technical Report* NPS-69-81-001, Naval Postgraduate School, Monterey, CA, 1981.
12. Felippa CA, DeRuntz JA. Acoustic fluid volume modeling by the displacement potential formulation, with emphasis on the wedge element. *Computers and Structures* 1991; **41**(4):669–686.
13. Sprague MA, Geers TL. Computational treatment of cavitation effects in near-free-surface underwater shock analysis. *Shock and Vibration* 2001; **8**(2):105–122.
14. Shin YS, Santiago LD. Surface ship shock modeling and simulation: two-dimensional analysis. *Shock and Vibration* 1998; **5**:129–137.
15. Almroth BO, Brogan FA, Stanley GS. Structural analysis of general shells: user instructions for STAGSC. *Technical Report* LMSC-D633873, Lockheed Palo Alto Research Laboratory, Palo Alto, CA, 1980.
16. Geers TL. Residual potential and approximate methods for three-dimensional fluid–structure interaction problems. *Journal of the Acoustical Society of America* 1971; **49**:1505–1510.
17. Geers TL. Doubly asymptotic approximations for transient motions of submerged structures. *Journal of the Acoustical Society of America* 1978; **64**(5):1500–1508.
18. DeRuntz JA. The underwater shock analysis code and its applications. In *Proceedings of the 60th Shock and Vibration Symposium*, Virginia Beach, VA, 1989.
19. Felippa CA, Park KC. Staggered solution transient analysis procedures for coupled mechanical systems. *Computer Methods in Applied Mechanics and Engineering* 1980; **20**:61–111.
20. MSC. *MSC/NASTRAN Quick Reference Guide*, *Version 67*. 1993.
21. Hallquist JO. *LS-DYNA User's Manual* (*Nonlinear Dynamic Analysis of Solids in Three Dimensions*). Livermore Software Technology Corporation, 1990. Report No. 1007.
22. Hibbitt, Karlsson, and Sorensen, Inc. *ABAQUS 6.2-1 Documentation*. 2001.
23. Cipolla JL. Personal communication, Hibbitt, Karlsson, and Sorensen, Inc., January 2002.
24. Mair HU. Review: hydrocodes for structural response to underwater explosions. *Shock and Vibration* 1999; **6**(2):81–96.
25. Marfurt KJ. Accuracy of finite-difference and finite-element modeling of the scalar and elastic wave equations. *Geophysics* 1984; **49**(5):533–549.
26. Sprague MA. Advances in computation methods for fluid–structure-interaction problems. *Master's Thesis*, University of Colorado at Boulder, 1999.
27. Hunter KS, Geers TL. Pressure and velocity fields produced by an underwater explosion. *Journal of the Acoustical Society of America* 2004; **115**(4):1483–1496.
28. Geers TL, Hunter KS. An integrated wave-effects model for an underwater explosion bubble. *Journal of the Acoustical Society of America* 2002; **111**(4):1584–1601.
29. Chan SK. A modified finite-element procedure for underwater shock analysis. In *Proceedings of the 61st Shock and Vibration Symposium*, vol. 3, San Diego, CA, 1990; 87–101.
30. Chan SK. An improvement in the modified finite-element procedure for underwater shock analysis. In *Proceedings of the 63rd Shock and Vibration Symposium*, SAVIAC, Arlington, VA, 1992; 616–627.
31. Taflove A, Hagness SC. *Computational Electrodynamics*: *The Finite-Difference Time-Domain Method*. Artech House: Boston, 2000.
32. Sprague MA, Geers TL. Spectral elements and field separation for an acoustic fluid subject to cavitation. *Journal of Computational Physics* 2003; **184**:149–162.

33. Cook RD, Malkus DS, Plesha ME. *Concepts and Applications of Finite Element Analysis*. Wiley: New York, 1989.
34. Mulder WA. Spurious modes in finite-element discretizations of the wave equation may not be all that bad. *Applied Numerical Mathematics* 1999; **30**:425–445.
35. Giannakouros J, Karniadakis GE. A spectral element-FCT method for the compressible euler equations. *Journal of Computational Physics* 1994; **115**:65–85.
36. Gottlieb D, Orszag SA. *Numerical Analysis of Spectral Methods: Theory and Applications*. SIAM: Philadelphia, PA, 1977.
37. Orszag SA. Spectral methods for problems in complex geometries. *Journal of Computational Physics* 1980; **37**:70–92.
38. Fornberg B. *A Practical Guide to Pseudospectral Methods*. Cambridge University Press: Cambridge, 1996.
39. Canuto C, Hussaini MY, Quarteroni A, Zang TA. *Spectral Methods in Fluid Dynamics*. Springer: New York, 1988.
40. Ronquist EM, Patera AT. A Legendre spectral element method for the Stefan problem. *International Journal for Numerical Methods in Engineering* 1987; **24**:2273–2299.
41. Maday Y, Patera AT. Spectral element methods for the incompressible Navier–Stokes equations. In *State-of-the-Art Surveys on Computational Mechanics*, Noor AK, Oden JT (eds). The American Society of Mechanical Engineers: New York, 1989; 71–142.
42. Komatitsch D, Vilotte JP. The spectral element method: an efficient tool to simulate the seismic response of 2D and 3D geological structures. *Bulletin of the Seismological Society of America* 1998; **88**(2):368–392.
43. Sidilkover D, Karniadakis GE. Non-oscillatory spectral element Chebyshev method for shock wave calculations. In *Fifth International Symposium on Domain Decomposition Methods for Partial Differential Equations* 1991; 566–585.
44. Yoon KT, Chung TJ. Three-dimensional mixed explicit-implicit generalized galerkin spectral element methods for high-speed turbulent compressible flows. *Computer Methods in Applied Mechanics and Engineering* 1996; **135**:343–367.
45. Giraldo FX. The Lagrange–Galerkin spectral element method on unstructured quadrilateral grids. *Journal of Computational Physics* 1998; **147**:114–146.
46. Fischer PF. Analysis and application of a parallel spectral element method for the solution of the Navier–Stokes equations. *Computer Methods in Applied Mechanics and Engineering* 1990; **80**:483–491.
47. Patera AT. A spectral element method for fluid dynamics: laminar flow in a channel expansion. *Journal of Computational Physics* 1984; **54**:468–488.
48. Ghaddar NK, Korczak KZ, Mikic BB, Patera AT. Numerical investigation of incompressible flow in grooved channels. Part 1. Stability and self-sustained oscillations. *Journal of Fluid Mechanics* 1986; **163**:99–127.
49. Padovani E, Priolo E, Seriani G. Low and high order finite-element method: experience in seismic modeling. *Journal of Computational Acoustics* 1994; **2**(4):371–422.
50. Priolo E, Carcione JM, Seriani G. Numerical simulation of interface waves by high-order spectral modeling techniques. *Journal of the Acoustical Society of America* 1994; **95**(2):681–693.
51. Seriani G, Priolo E. Spectral element method for acoustic wave simulation in heterogeneous media. *Finite Elements in Analysis and Design* 1994; **16**:337–348.
52. Maday Y, Ronquist EM. Optimal error analysis of spectral methods with emphasis on non-constant coefficients and deformed geometries. *Computer Methods in Applied Mechanics and Engineering* 1990; **80**:91–115.
53. Farhat C, Lesoinne M, LeTallec P. Load and motion transfer algorithms for fluid/structure interaction problems with non-matching discrete interfaces: momentum and energy conservation, optimal discretization and application to aeroelasticity. *Computer Methods in Applied Mechanics and Engineering* 1998; **157**:95–114.
54. Belgacem FB, Maday Y. Coupling spectral and finite-elements for second order elliptic three-dimensional equations. *SIAM Journal of Numerical Analysis* 1999; **36**(4):1234–1263.
55. Belytschko T, Yen HJ, Mullen R. Mixed methods for time integration. *Computer Methods in Applied Mechanics and Engineering* 1979; **17**:259–275.
56. Belytschko T. Partitioned and adaptive algorithms for explicit time integration. In *Nonlinear Finite Element Analysis in Structural Mechanics*, Wunderlich W, Stein E, Bath KJ (eds). Springer: Berlin, 1981; 572–584.
57. Hulbert GM Hughes TJR. Numerical evaluation and comparison of subcycling algorithms for structural dynamics. *Technical Report* DNA-TR-88-8, Defense Nuclear Agency, Washington, DC, 1988.
58. Acheson DJ. *Elementary Fluid Dynamics*. Oxford University Press: Oxford, 1990.
59. Deville MO, Mund EH, Fischer PF. *High-Order Methods for Incompressible Fluid Flow*. Cambridge University Press: Cambridge, 2002.

60. Fischer PF. Personal communication, May 2002.
61. Sprague MA. Advanced Computational Techniques for the Analysis of 3D Fluid-Structure Interaction with Cavitation. *Ph.D. Thesis*, University of Colorado at Boulder, 2002.
62. Felippa CA. A family of early-time approximations for fluid–structure interaction. *Journal of Applied Mechanics* 1980; **47**:703–708.
63. DeRuntz JA, Geers TL, Felippa CA. The underwater shock analysis (USA-version 3) code, a reference manual. *Technical Report* DNA 5615F, Defense Nuclear Agency, Washington, DC, September 1980.
64. Belytschko T. An overview of semidiscretization and time integration procedures. In *Computational Methods for Transient Analysis*, Belytschko T, Hughes TJR (eds). North-Holland, Amsterdam, 1983.
65. Iserles A. *A First Course in the Numerical Analysis of Differential Equations*. Cambridge University Press: Cambridge, 1996.
66. Geers TL. An objective error measure for the comparison of calculated and measured transient response histories. *The Shock and Vibration Bulletin* 1984; **54**:99–107.
67. Swisdak MM (ed.). *Explosion Effects and Properties: Part II—Explosion Effects in Water*. NSWC/WOL TR 76-116. NSWC, February 1978.
68. Zhang P, Geers TL. Excitation of a fluid-filled, submerged spherical shell by a transient acoustic wave. *Journal of the Acoustical Society of America* 1993; **93**(2):696–705.
69. Geers TL, Ju T. A computer program for a canonical problem in underwater shock. *Shock and Vibration* 1994; **1**(4):331–337.
70. Sprague MA, Geers TL. Response of empty and fluid-filled, submerged spherical shells to plane and spherical, step-exponential acoustic waves. *Shock and Vibration* 1999; **6**:147–157.

